A&A 645, A33 (2021)
https://doi.org/10.1051/0004-6361/202039057
© ESO 2020

Astronomy & Astrophysics

The WISSH quasars project

IX. Cold gas content and environment of luminous QSOs at $z \sim 2.4$–4.7

M. Bischetti[1,2], C. Feruglio[1], E. Piconcelli[2], F. Duras[3,2], M. Pérez-Torres[4,5], R. Herrero[6,7], G. Venturi[8], S. Carniani[9], G. Bruni[10], I. Gavignaud[11], V. Testa[2], A. Bongiorno[2], M. Brusa[12,13], C. Circosta[14], G. Cresci[15], V. D'Odorico[1,9], R. Maiolino[16,17], A. Marconi[18,15], M. Mingozzi[19], C. Pappalardo[20], M. Perna[21,15], E. Traianou[22], A. Travascio[2], G. Vietri[23], L. Zappacosta[2], and F. Fiore[1]

(Affiliations can be found after the references)

Received 29 July 2020 / Accepted 10 October 2020

ABSTRACT

Context. Sources at the brightest end of the quasi-stellar object (QSO) luminosity function, during the peak epoch in the history of star formation and black hole accretion ($z \sim 2$–4, often referred to as "Cosmic noon") are privileged sites to study the cycle of feeding & feedback processes in massive galaxies.

Aims. We aim to perform the first systematic study of cold gas properties in the most luminous QSOs, by characterising their host-galaxies and environment. These targets exhibit indeed widespread evidence of outflows at nuclear and galactic scales.

Methods. We analyse ALMA, NOEMA and JVLA observations of the far-infrared continuum, CO and [CII] emission lines in eight QSOs (bolometric luminosity $L_{\rm Bol} \gtrsim 3 \times 10^{47}$ erg s^{-1}) from the WISE-SDSS selected hyper-luminous (WISSH) QSOs sample at $z \sim 2.4$–4.7.

Results. We report a 100% emission line detection rate and a 80% detection rate in continuum emission, and we find CO emission to be consistent with the steepest CO ladders observed so far. Sub-millimetre data reveal presence of (one or more) bright companion galaxies around ∼80% of WISSH QSOs, at projected distances of ∼6−130 kpc. We observe a variety of sizes for the molecular gas reservoirs (∼1.7−10 kpc), mostly associated with rotating disks with disturbed kinematics. WISSH QSOs typically show lower CO luminosity and higher star formation efficiency than infrared matched, $z \sim 0$–3 main-sequence galaxies, implying that, given the observed SFR ∼170−1100 $M_\odot$ yr^{-1}, molecular gas is converted into stars in ≲50 Myr. Most targets show extreme dynamical to black-hole mass ratios $M_{\rm dyn}/M_{\rm BH} \sim 3$–$10$, two orders of magnitude smaller than local relations. The molecular gas fraction in the host-galaxies of WISSH is lower by a factor of ∼10−100 than in star forming galaxies with similar M_*.

Conclusions. Our analysis reveals that hyper-luminous QSOs at Cosmic noon undergo an intense growth phase of both the central super-massive black hole and of the host-galaxy. These systems pinpoint the high-density sites where giant galaxies assemble, where we show that mergers play a major role in the build-up of the final host-galaxy mass. We suggest that the observed low molecular gas fraction and short depletion timescale are due to AGN feedback, whose presence is indicated by fast AGN-driven ionised outflows in all our targets.

Key words. galaxies: high-redshift – galaxies: ISM – techniques: interferometric – quasars: supermassive black holes – submillimeter: galaxies – quasars: emission lines

1. Introduction

Our understanding of the complex interplay between super-massive black hole (SMBH) activity, properties of the host-galaxy interstellar medium (ISM) and of the circum-galactic environment is still incomplete. According to models of active galactic nucleus (AGN) and galaxy co-evolution, two main processes are expected to drive the evolution of massive galaxies (stellar mass $M_* > 10^{11}\,M_\odot$): (i) galaxy interactions and mergers, and (ii) radiative and mechanical feedback related to AGN activity (e.g. Croton et al. 2006; Sijacki et al. 2007; Martín-Navarro et al. 2018; Choi et al. 2018), during the growth of heavy SMBHs ($M_{\rm BH}/M_* \sim 10^{-3}$, where $M_{\rm BH}$ is the black hole mass, e.g. Häring & Rix 2004). These two processes are tightly correlated, as galaxy interactions destabilise the gas and make it available fuel for both star formation (SF) and nuclear accretion (e.g. Volonteri et al. 2015; Anglés-Alcázar et al. 2017). In turn, powerful AGN-driven, galaxy-scale outflows can hamper further SF and nuclear gas accretion by injecting energy and entropy into the host-galaxy ISM (e.g. King & Pounds 2015; Richings & Faucher-Giguère 2018; Menci et al. 2019) and circum-galactic environment (van de Voort 2017; Travascio et al. 2020).

It is crucial to probe the cycle of feeding & feedback processes in massive galaxies and the AGN-galaxy co-evolution during Cosmic noon ($z \sim 2$–4.5), that is the peak epoch of galaxy assembly and SMBH accretion. Indeed, hyper-luminous quasi-stellar object (QSOs, bolometric luminosity $L_{\rm Bol} > 10^{47}$ erg s^{-1}) are preferred targets, being powered by massive ($M_{\rm BH} \gtrsim 10^9\,M_\odot$), highly accreting SMBHs (Banerji et al. 2015; Shen 2016; Vietri et al. 2018). These heavy SMBHs have been found to reside in most local giant elliptical galaxies (Kormendy & Ho 2013; Shankar et al. 2019), although most of their mass has been assembled at early times during bright AGN phases (e.g. Marconi et al. 2004; Delvecchio et al. 2014). Giant ellipticals have also built most of their stellar mass at $z \gtrsim 2$ (∼80% for sources with $M_* > 10^{11}\,M_\odot$) and then rapidly evolved off the galaxy Main Sequence (MS) becoming "red & dead" (e.g. Santini et al. 2009; McDermid et al. 2015). Overall, this strongly suggests that high-z, hyper-luminous QSOs are the assembly sites of giant galaxies. Indeed, the huge luminosities of these QSOs are likely triggered by galaxy

interactions (e.g. Urrutia et al. 2008; Menci et al. 2014), and drive powerful outflows which may affect the host-galaxy (Carniani et al. 2015; Zakamska et al. 2016; Bischetti et al. 2017, 2019a; Perrotta et al. 2019; Villar Martín et al. 2020; Herrera-Camus et al. 2020).

Investigating the properties of the cold ISM (that is the raw material of SF) in objects at the brightest end of the QSO luminosity function is mandatory to constrain the impact of AGN activity on the host-galaxy evolution. Our knowledge of the host-galaxies of $z > 1$ QSOs has been revolutionised by interferometric observations at sub-millimetre wavelengths. Specifically, CO rotational emission is the most targeted transition in $z \lesssim 4$ QSOs and probes the molecular gas reservoir. At higher redshift, it is possible to more easily exploit the bright [CII] fine structure emission line at $\lambda 158\,\mu$m, which is mostly associated with cold neutral gas (Solomon & Vanden Bout 2005; Carilli & Walter 2013; Zanella et al. 2018; Veilleux et al. 2020). Previous studies of luminous QSOs at $z \sim 2$–6 revealed a variety of host-galaxy properties. These sources typically reside in compact hosts, in some of which rotating disks are in place, while others show irregular morphology and disturbed kinematics (Díaz-Santos et al. 2016; Banerji et al. 2017; Brusa et al. 2018; Feruglio et al. 2018; Talia et al. 2018; Pensabene et al. 2020). Intense SF activity of hundreds to thousands solar masses per year is usually observed (Maiolino et al. 2012; Duras et al. 2017; Fan et al. 2019; Nguyen et al. 2020), although it is unclear whether this is linked to galaxy interactions (Trakhtenbrot et al. 2017; Bischetti et al. 2018; Fan et al. 2018, 2019).

While great emphasis has been put in uncovering the formation and early growth of QSOs and their host-galaxies at $5 \lesssim z \lesssim 7$ (e.g. Wang et al. 2013, 2016; Decarli et al. 2018; Venemans et al. 2017a, 2019; Bañados et al. 2019), currently there is a lack of systematic investigation into the ISM and environment properties of QSOs shining at Cosmic noon. There is a series of works based on individual, often gravitationally-lensed sources (e.g. Carilli & Walter 2013, and references therein) or peculiar AGN types, such as heavily-reddened and hot, dust-obscured QSOs (e.g. Banerji et al. 2017; Fan et al. 2018). Few studies, based on heterogeneous samples including QSOs with different selection criteria (Feruglio et al. 2014; Perna et al. 2018) suggested a typically higher star formation efficiency (SFE) in QSOs, defined as the rate of SF per unit of molecular gas mass, with respect to non-active sources on the galaxy MS, although e.g. Kirkpatrick et al. (2019) found no significant correlation between the SFE and the AGN fraction at mid-infrared wavelengths. An increased SFE in QSOs is expected in the standard paradigm of a QSO expelling/heating gas from the host-galaxy in the transitory phase from starburst to blue QSO (Di Matteo et al. 2007; Hopkins 2012). Indeed, few works probing the molecular gas content in $z \sim 1.5$–2.5 QSOs with known presence of AGN-driven outflows reported a lower molecular gas content with respect to MS galaxies (Brusa et al. 2015, 2018; Carniani et al. 2017; Kakkad et al. 2017), while others found no difference (e.g. Herrera-Camus et al. 2019).

In this framework, we have undertaken the WISE-SDSS selected hyper-luminous (WISSH) QSOs project to study the most powerful AGN in the Universe, which happen to shine at Cosmic noon and show widespread evidence of strong, AGN-driven outflows on nuclear to circum-galactic scales (Bischetti et al. 2017; Vietri et al. 2018; Bruni et al. 2019; Travascio et al. 2020). These QSOs are therefore ideal targets to shed light on the AGN-galaxy feeding and feedback cycle. In this work, we present sub-millimetre and millimetre observations of eight WISSH QSOs at $z \sim 2.4$–4.7 to probe SMBH and galaxy assembly at the massive end of the mass function and investigate the interplay between nuclear activity and the physical properties of the host-galaxy ISM.

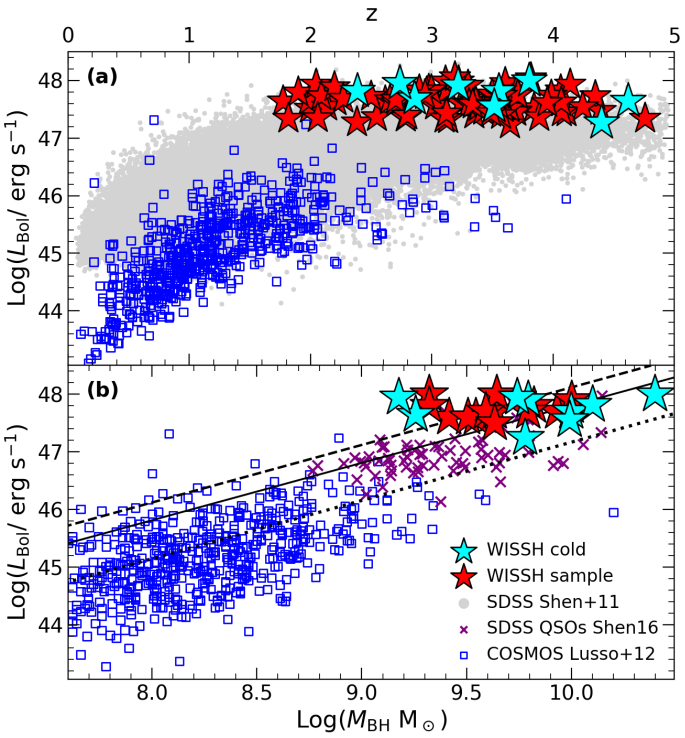

Fig. 1. *Panel a*: bolometric luminosity as a function of redshift for the total WISSH sample, compared to SDSS QSOs from Shen et al. (2011) and COSMOS QSOs from Lusso et al. (2012). Cyan stars indicate WISSH QSOs with (sub-)millimetre observations. *Panel b*: bolometric luminosity vs. black hole mass. We include WISSH QSOs with Hβ-based $M_{\rm BH}$ from Vietri et al. (2018) and luminous SDSS QSOs from Shen (2016). Lines correspond to $L_{\rm Bol}/L_{\rm Edd} = 1$ (dashed), $L_{\rm Bol}/L_{\rm Edd} = 0.5$ (solid), and $L_{\rm Bol}/L_{\rm Edd} = 0.1$ (dotted).

The paper is organised as follows. In Sect. 2 we describe the targets and the (sub-)millimetre observations, detailing data reduction and analysis in Sect. 2.2. The main results are presented in Sect. 3, focusing on continuum (3.1), CO and [CII] emission (3.2). The CO spectral line energy distribution (SLED) and the UV-to-FIR spectral energy distribution (SED) are described in Sects. 3.3 and 4. Section 5 is dedicated to the cold gas kinematics. We discuss environment, star-formation efficiency, gas excitation, dynamical mass and molecular gas fraction of WISSH QSOs in Sect. 6. Finally, our conclusions are summarised in Sect. 7.

Throughout this paper, we assume a ΛCDM cosmology with $H_0 = 67.3\,{\rm km\,s^{-1}\,Mpc^{-1}}$, $\Omega_\Lambda = 0.69$ and $\Omega_{\rm M} = 0.31$ (Planck Collaboration XIII 2016).

2. Sample and observations

2.1. Sample description

The targets presented in this work are drawn from the WISSH QSOs sample (Bischetti et al. 2017), including 86 hyper-luminous, Type I QSOs at $z \sim 1.8$–4.8, selected to have a flux density $S_{22\,\mu{\rm m}} > 3$ mJy by cross correlating the WISE all sky source catalogue with the SDSS DR7 catalogue. As shown in Fig. 1a, the WISSH sample collects the most luminous AGN known, characterised by bolometric luminosities

Table 1. Journal of observations.

ID	RA	Dec	z_{SDSS}	Telescope	Transition	Beamsize (arcsec^2)	ν_{cont} (GHz)	$\sigma_{40\,km\,s^{-1}}$ (mJy beam^{-1})	σ_{cont} (mJy beam^{-1})
(1)	(2)	(3)	(4)	(5)	(6)	(7)	(8)	(9)	(10)
J0209−0005	02:09:50.71	−00:05:06.22	2.849	NOEMA	CO(5−4)	4.9×2.7	148.7	0.90	0.040
				JVLA	CO(1−0)	3.1×2.3	31.6	0.08	0.005
J0801+5210	08:01:17.82	+52:10:34.94	3.217	NOEMA	CO(5−4)	3.8×1.9	136.6	1.05	0.100
				JVLA	CO(1−0)	3.4×2.3	30.2	0.16	0.010
J1433+0227	14:33:52.21	+02:27:14.01	4.622	ALMA	[CII]	0.44×0.34	338.1	0.43	0.051
J1538+0855	15:38:30.49	+08:55:17.42	3.542	ALMA	CO(4−3)	1.1×0.7	94.3	0.49	0.028
J1549+1245	15:49:38.71	+12:45:09.25	2.386	ALMA	CO(4−3)	1.0×0.9	141.8	0.10	0.007
J1555+1003	15:55:14.86	+10:03:51.23	3.512	ALMA	CO(4−3)	1.0×0.7	94.30	0.57	0.028
J1639+2824	16:39:09.11	+28:24:47.16	3.786	ALMA	CO(4−3)	0.20×0.13	100.4	0.43	0.026
J1701+6412	17:01:00.60	+64:12:09.32	2.724	NOEMA	CO(5−4)	4.0×2.1	154.7	1.03	0.100
J1015+0020 (*)	10:15:49.00	+00:20:20.03	4.400	ALMA	[CII]	0.22×0.18	357.3	0.19	0.040

Notes. Columns give the following information: (1) SDSS ID, (2) and (3) Celestial coordinates, (4) Redshift based on SDSS DR12 (Alam et al. 2015), (5) Observation telescope, (6) Observed transition, (7) Angular resolution, (8) Observed continuum frequency, (9) rms sensitivity for a channel width of 40 km s^{-1}, and (10) Continuum rms sensitivity. (*)Presented in Bischetti et al. (2018).

$L_{Bol} > 10^{47}$ erg s^{-1} (Duras et al. 2017). The selection of Type 1 SDSS QSOs includes sources affected by low-moderate extinction (Duras et al. 2017), for a large fraction of which we collected reliable estimates of the SMBH mass via broad emission line-widths. Near-IR spectroscopy revealed that WISSH QSOs are powered by highly accreting SMBHs (accretion rate $\lambda_{Edd} = L_{Bol}/L_{Edd} \simeq 0.4-3$ (Fig. 1b), where L_{Edd} is the Eddington luminosity) with typical masses $M_{BH} > 2 \times 10^9\,M_\odot$ (Bischetti et al. 2017, 2018; Vietri et al. 2018).

Here we present observations of WISSH QSOs performed with the Atacama Large Millimetre/submillimetre Array (ALMA), the Northern Emisphere Millimetre Array (NOEMA), and the *Karl G. Jansky* Very Large Array (JVLA). We include ALMA band 3 data from projects 2013.1.00417.S (P.I. I. Gavignaud) and 2019.1.01070.S (P.I. G. Venturi), and band 7 data from project 2016.1.00718.S (P.I. F. Fiore); NOEMA band 2 data from projects S17BW and W17DT (P.I. G. Bruni) and JVLA Ka band data from project VLA/18A−028 (P.I. M. Bischetti). We also collected all publicly available archival data from the ALMA archive as of December 2019, including ALMA projects 2015.1.01602.S (band 3, P.I. M. Schramm), 2016.1.01515.S (band 7, P.I. P. Lira), and ACA project 2018.1.01806.S (band 6, P.I. K. Hall).

The combination of these projects has provided us with observations of sub-millimetre to centimetre continuum (observed frequency range ∼350−30 GHz) and cold gas emission for a sample of nine WISSH QSOs (Fig. 1). Specifically, CO rotational emission is available for seven targets at $z \sim 2.7-3.8$, including CO(4−3)($\nu_{rest} = 461.04$ GHz) and CO(5−4)($\nu_{rest} = 576.27$ GHz) transitions, as listed in Table 1. For two QSOs, namely J0209–0005 and J0801+5210, we have combined information about the ground transition CO(1−0)($\nu_{rest} = 115.27$ GHz) and CO(5−4). Moreover, we have collected observations of the [CII]($\nu_{rest} = 1900.54$ GHz) fine structure emission line for two WISSH QSOs at $z > 4$. The results about J1015+0020 at $z \sim 4.4$ were presented in Bischetti et al. (2018), while in this work we analyse J1433+0227 at $z \sim 4.7$ (see also Nguyen et al. 2020).

The sub-sample of WISSH QSOs analysed here derives from different projects, originally designed with different purposes. The three targets J1538+0855, J1549+1245 and J1555+1003 were selected to have AGN-driven outflows in the ionised gas phase (Bischetti et al. 2017; Vietri et al. 2018). Our analysis revealed that all WISSH QSOs in which we investigated the presence of [OIII] or CIV outflows satisfy this criterion (Vietri et al. 2018). These three QSOs (out of nine targets) also show broad absorption line (BAL) features in their UV spectra, consistently with the BAL fraction of ∼25% measured for the parent WISSH sample by Bruni et al. (2019). Targets J0209–0005, J0801+5210, J1433+0227, J1701+6412 (and J1015+0020 in Bischetti et al. 2018) were chosen to be detected by *Herschel*/SPIRE photometry in the far-infrared. Nevertheless, ∼90% of WISSH QSOs with *Herschel*/SPIRE coverage are detected (Duras et al. 2017). The QSO J1639+2824 was selected to have a nearby bright star, suitable for adaptive optics (AO)-assisted observations, in order to perform a joint Subaru and ALMA study of the host galaxy properties and of the SMBH-galaxy mass ratio (Schramm et al. 2019). Figure 1a shows that our targets well represent the z and L_{Bol} range covered by the total WISSH sample. Similarly, their M_{BH} span over a similar interval than that covered by WISSH QSOs with Hβ-based M_{BH} (Vietri et al. 2018), except for the more massive SMBH in J1639+2824 (Fig. 1b). We note that the M_{BH} of J0801+5210, J1538+0855 and J1549+1245 is derived from the Hβ emission line (Vietri et al. 2018), that of J1433+0227 is MgII-based (Trakhtenbrot et al. 2011), while the M_{BH} of the remaining targets is CIV-based (Weedman et al. 2012) and corrected for the presence of CIV outflows (Coatman et al. 2017). Globally, the selection of our targets does not introduce strong biases and the results of the following analysis can be considered as representative of the total WISSH sample.

2.2. Data reduction and analysis

ALMA data were calibrated using the CASA software (McMullin et al. 2007) in the pipeline mode. For each source, we used the CASA version indicated by the ALMA observatory and the default phase, bandpass and flux calibrators. The absolute flux accuracy is better than 10%. To estimate the far-IR continuum emission, we averaged visibilities over all spectral windows excluding the spectral range covered by CO or [CII] emission lines, for a total of ∼7 GHz. Moreover, to model the continuum emission next to the line, we combined the adjacent spectral windows in the ALMA baseband containing CO or [CII]. We performed a fit in the *uv* plane to all channels with velocity $|v| > 500$ km s^{-1} by adopting a first order polynomial continuum

model. We subtracted this fit to produce continuum-subtracted visibilities.

Continuum-subtracted data cubes were created with the CASA 5.4.0 task *tclean*, using the *hogbom* cleaning algorithm (Högbom 1974) in non-interactive mode, and a threshold equal to three times the rms sensitivity. For all sources except J1639+2824, a natural weighting of the visibilities and a common spectral channel width of 40 km s^{-1} were chosen. The same deconvolution procedure was adopted to produce continuum maps. In the case of J1639+2824, we applied a tapering of the visibilities beyond 900 kλ, corresponding to a baseline length $\gtrsim$2800 km, to decrease the very high native resolution (0.11×0.06 arcsec^2) to a tapered beam of 0.20×0.13 arcsec^2. This resulted into a higher significance of CO(4−3) detection by a factor of ∼1.5, similarly to what found by Schramm et al. (2019) for this QSO.

Regarding NOEMA data, project S17BW was acquired with the WideX correlator and span a total spectral range of ∼4 GHz, while project W17DT was obtained with the PolyFiX correlator and span a wider spectral interval of ∼14 GHz. We calibrated the visibilities using the CLIC pipeline of the GILDAS software[1]. The absolute flux accuracy is better than 10%. Imaging was performed with MAPPING, following the same procedure described above for ALMA observations.

Given the redshift of J0209–0005 and J0801+5210, we used JVLA *Ka*-band observations. We observed each QSO using two separate windows of eight 128 MHz wide sub-bands for a total bandwidth of 1 GHz per window. Each sub-band had a native spectral resolution of 1 MHz. We calibrated the visibilities, both continuum and spectral line CO(1−0), following standard procedures within the CASA software package. The absolute flux accuracy is better than 15%. We imaged our sources using the CASA task tclean, following the same procedures applied to our ALMA data. Table 1 presents the journal of observations. For each target, we list the resulting beamsize, the rms sensitivity of the datacube for a channel width of 40 km s^{-1} ($\sigma_{40\,\mathrm{km\,s^{-1}}}$) and the rms sensitivity of the continuum map ($\sigma_{\rm cont}$).

To derive flux density and size of the continuum emission in our targets, we (i) fitted the data in the image plane with a two-dimensional Gaussian profile by using CASA task *imfit*, and (ii) performed a fit of the visibilities in the *uv* plane with MAPPING task uvfit. In (ii), channels associated with the continuum emission, were spectrally and temporally averaged (to 30 s). We then fitted point source or Gaussian source models to the visibilities. In the case of multiple sources, we first fitted and subtracted emission from the QSO host-galaxy, then fitted emission from nearby emitters. A Gaussian model was preferred when resulting into an increased significance of the detection and a size different from null size at $>3\sigma$ (where σ is the error associated with the Gaussian axis derived from the fit in the *uv* plane). We checked that subtracting the models resulted into uniform residual noise maps. Similarly, we measured the integrated CO or [CII] flux density by averaging channels related to line emission (filled histogram in Fig. 4) and fitting the data in both image and *uv* plane. We verified that (i) and (ii) give consistent sizes and flux density values.

One-dimensional spectra were extracted from the continuum-subtracted datacubes from a region centred on the peak of CO or [CII] integrated flux density, including emission detected at $S/N > 2$. Given the modest signal-to-noise ratio of most spectra (see Fig. 4), we fitted them with a Gaussian profile by using the python package scipy.optimize.curve_fit leaving all parameters free to vary. We verified that by fitting the spectra with a two-Gaussian model, the line significance and parameters were consistent within the uncertainties with the single Gaussian fit. This provided us with FWHM and centroid of the emission line profiles, which was used to infer the CO or [CII] based redshift ($z_{\rm cold}$) of our targets listed in Table 2.

[1] www.iram.fr/IRAMFR/GILDAS

3. Results from sub-mm and mm observations

3.1. Continuum emission

Figure 2 shows the (sub-)millimetre continuum maps for the eight WISSH QSOs analysed in this work. Observed ∼90−340 GHz (rest-frame ∼430−1935 GHz) continuum emission is detected at $>4\sigma_{\rm cont}$ significance in five out of eight sources (namely J0209–0005, J1433+0227, J1549+1245, J1555+1003, and J1701+6412) while emission is observed at $\sim3\sigma_{\rm cont}$ significance at the location of the QSO in J0801+5210 and J1639+2824. We also detect rest-frame ∼125 GHz continuum in the JVLA maps of J0209–0005 and J0801+5210 at $\sim8\sigma_{\rm cont}$ and $\sim9\sigma_{\rm cont}$ significance, respectively. Measured continuum flux densities range from ∼0.04 mJy at rest-frame 125 GHz to ∼0.1 mJy at 460 GHz and ∼0.6 mJy at 580 GHz (Table 2). For the WISSH QSO J1433+0227 we measure a strong rest-frame 1935 GHz continuum flux density of 7.7 ± 0.3 mJy. The latter is a factor of ∼10 higher than the 1935 GHz continuum flux density found for the WISSH QSO J1015+0020 at $z \sim 4.4$ in Bischetti et al. (2018), suggesting a large variety of far-infrared continuum properties in our sample, similarly to what observed in $z \sim 5$−6 QSOs (e.g. Trakhtenbrot et al. 2017; Nguyen et al. 2020).

The limited angular resolution of most observations presented in this work hampers a detailed study of the continuum emission morphology in these QSOs. Continuum morphology is consistent with a point source in all targets except J1433+0227 and J1549+1245, for which we measure a deconvolved angular size of $(0.31 \pm 0.02) \times (0.27 \pm 0.02)$ arcsec^2 and $(0.69 \pm 0.19) \times (0.50 \pm 0.20)$ arcsec^2, corresponding to $\sim2.0 \times 1.8$ kpc and $\sim5.7 \times 4.2$ kpc^2, respectively.

In the field of view of J1549+1245, a strong continuum emitter is detected at ∼2.4 arcsec from the nucleus (Fig. 2e), associated with a companion source (see Sect. 3.2) whose continuum emission is comparable to that of the QSO host-galaxy, with a size of $(0.74 \pm 0.22) \times (0.43 \pm 0.23)$ arcsec^2, corresponding to $\sim6.1 \times 3.6$ kpc^2. Weak, elongated continuum emission can be also observed along the QSO-companion direction, possibly linked to a tidal feature. Also in J0209–0005, the elongated continuum structure which can be observed at $\sim5\sigma_{\rm cont}$ in the north-east direction, up to ∼5 arcsec from the nucleus, reveals the presence of a continuum-emitting nearby source (see Sect. 3.2) whose continuum flux is about 45% of that of the QSO.

3.2. CO and [CII] emission

Figure 3 shows the continuum-subtracted, velocity-integrated maps of CO and [CII] emission for the eight WISSH QSOs analysed in this work. The detection rate in mid-*J* CO and [CII] emission is 100% with significance of ~4.5−$30\sigma_{\rm cold}$, where $\sigma_{\rm cold}$ is the rms sensitivity (also given in Fig. 3) of the velocity-integrated emission line maps. CO(1−0) is also detected at $\sim5\sigma_{\rm cold}$ in one of the two WISSH QSOs targeted by JVLA, namely J0209–0005, while no significant CO(1−0) emission is observed in J0801+5210. In Fig. 3, the location of the maximum FIR continuum emission (or the optical position of the

Table 2. Properties of continuum and line (CO or [CII]) emission for the WISSH QSOs analysed here.

ID	Transition	$z_{\rm cold}$	*FWHM* (km s^{-1})	$S\Delta v$ (Jy km s^{-1})	$L'_{\rm CO}$ (10^{10} K km s^{-1} pc^2)	$L_{\rm [CII]}$ (10^9 $L_\odot$)	$S_{\rm cont}$ (mJy)
(1)	(2)	(3)	(4)	(5)	(6)	(7)	(8)
J0209–0005	CO(5–4)	2.870	435 ± 95	1.4 ± 0.3	2.15 ± 0.46	–	0.38 ± 0.04
	CO(1–0)	2.870	440 ± 85	0.062 ± 0.012	2.39 ± 0.46	–	0.039 ± 0.005
J0801+5210	CO(5–4)	3.256	685 ± 70	3.68 ± 0.40	6.99 ± 0.76	–	<0.30 [b]
	CO(1–0)	–	–	<0.095 [a]	<4.48	–	0.091 ± 0.010
J1433+0227	[CII]	4.728	400 ± 40	5.40 ± 0.24	–	3.72 ± 0.16	7.7 ± 0.3
J1538+0855	CO(4–3)	3.572	320 ± 90	0.36 ± 0.11	1.23 ± 0.38	–	<0.087 [b]
J1549+1245	CO(4–3)	2.374	245 ± 40	0.27 ± 0.03	0.47 ± 0.05	–	0.12 ± 0.01
J1555+1003	CO(4–3)	3.529	605 ± 90	0.87 ± 0.14	2.94 ± 0.68	–	0.10 ± 0.02
J1639+2824	CO(4–3)	3.846	615 ± 90	0.92 ± 0.15	3.55 ± 0.66	–	<0.090 [b]
J1701+6412	CO(5–4)	2.753	595 ± 120	1.50 ± 0.34	2.15 ± 0.49	–	0.60 ± 0.06
J1015+0020 [*]	[CII]	4.407	340 ± 40	0.47 ± 0.05	–	0.29 ± 0.03	0.60 ± 0.06
Comp$_{\rm J0209}$	CO(5–4)	2.881	600 ± 95	1.1 ± 0.3	1.74 ± 0.46	–	0.14 ± 0.03
	CO(1–0)	–	–	<0.044 [a]	<1.71	–	<0.014 [b]
Comp$_{\rm J0801}$	CO(5–4)	3.271	385 ± 65	0.71 ± 0.26	1.36 ± 0.49	–	<0.30 [b]
	CO(1–0)	–	–	<0.058 [a]	<2.78	–	<0.30 [b]
Comp$_{\rm J1433}$	[CII]	4.728	100 ± 43	0.11 ± 0.02	–	0.08 ± 0.02	<0.015 [b]
Comp1$_{\rm J1549}$	CO(4–3)	2.363	540 ± 95	0.29 ± 0.05	0.49 ± 0.08	–	0.12±0.01
Comp2$_{\rm J1549}$	CO(4–3)	2.374	540 ± 110	0.046 ± 0.013	0.08 ± 0.02	–	<0.021 [b]
Comp$_{\rm J1555}$	CO(4–3)	3.531	370 ± 70	0.29 ± 0.06	0.98 ± 0.20	–	<0.084 [b]
Comp$_{\rm J1701}$	CO(5–4)	2.753	130 ± 60	0.50 ± 0.19	0.84 ± 0.27	–	<0.30 [b]

Notes. Columns give the following information: (1) SDSS ID, (2) Observed transition, (3) Redshift estimated from (sub-)mm emission lines with typical uncertainty $\Delta z_{\rm cold} \sim 0.001$, (4) and (5) FWHM and integrated flux of CO or [CII], (6) CO luminosity, (7) [CII] luminosity and (8) Continuum flux. Uncertainties do not include errors on abso. [*]Presented in Bischetti et al. (2018). [a]Upper limit computed for a point source as $3\times\sigma_{\rm cold}$, where $\sigma_{\rm cold}$ is the rms of the velocity integrated JVLA map produced by assuming the same FWHM of CO(5–4). [b]Upper limit computed for a point source as $3\times\sigma_{\rm cont}$ (Table 1).

QSO, in the case of continuum-undetected sources J1538+0855 and J1639+2824) is also shown by yellow (red) stars. For most sources, a small offset between continuum and CO or [CII] emission can be observed, typically smaller than 0.5 arcsec. The largest offset, that is ∼1 arcsec, is observed between the SDSS optical position and the peak of CO(4–3) emission in J1538+0855, although consistent within the uncertainty on the optical coordinates.

In addition to cold gas emission from the host-galaxies of the WISSH QSOs, CO and [CII] maps revealed the presence of several line emitters detected within an angular separation of ∼0.8 arcsec up to ∼16 arcsec from the nuclei, as shown by coloured contours in Fig. 3. Specifically, six out of eight WISSH QSOs analysed here show line emitters within the ALMA or NOEMA field of view, detected at $\gtrsim 5\sigma_{\rm cold}$ significance. Two of them, namely Comp$_{\rm J0209}$ and Comp$_{\rm J1549}$, are also detected in continuum emission (Sect. 3.1). For each of these sources, the proximity to the QSO in terms of sky frequency of the line emission (corresponding to a velocity shift in the range ∼40–1800 km s^{-1}) and angular separation suggests that they are companion CO and [CII] emitters, located at approximately the same redshift of the QSO.

Figure 4 shows the continuum-subtracted CO and [CII] spectra of the eight WISSH QSOs and of their companion galaxies, extracted from regions where line emission is detected at $>2\sigma_{\rm cold}$ in the QSO host-galaxy. For each source, the best-fit Gaussian model of the line is also displayed by the red curve. The redshift inferred from the Gaussian centroid ($z_{\rm cold}$), the FWHM and integrated flux density for each line are listed in Table 2. Details about individual QSOs are given below.

J0209–0005. This QSO has been detected in both CO(5–4) and CO(1–0) emission in the NOEMA and JVLA maps (Fig. 3a). At the resolution and sensitivity of our observations, both transitions show a morphology which is consistent with a point source, although a low-significance tail can be observed in CO(1–0) south of the QSO location. Redshift and line width estimates based on CO(5–4) and CO(1–0) are consistent within the uncertainties. A strong CO(5–4) emitting companion is located north-east of the QSO at an angular separation of ∼4 arcsec, corresponding to a projected distance of ∼32 kpc at the redshift of the QSO. It shows a broad CO(5–4) profile, redshifted by ∼800 km s^{-1} with respect to the QSO. Continuum emission associated with the companion can be also seen at ∼150 GHz in the observed frame, as the elongated structure in Fig. 2a.

J0801+5210. Although characterised by a bright CO(5–4) emission with a peak flux density of 5 mJy, this source shows no detected CO(1–0) in the JVLA map (Fig. 3b). To infer an upper limit on the CO(1–0) integrated flux density $S\Delta v_{1-0}$, we have integrated the JVLA datacubes around $z_{\rm cold}$ over 685 km s^{-1}, assuming the same FWHM of CO(5–4). We have then computed $S\Delta v_{1-0} = 3\times\sigma_{\rm CO,1-0}$, where $\sigma_{\rm CO,1-0}$ is the rms sensitivity of the velocity-integrated CO(1–0) map (Table 2). In the NOEMA map, a nearby source emitting in CO(5–4) can be also seen at a projected distance of ∼40 kpc from J0801+5210.

J1433+0227. This QSO at $z_{\rm cold} = 4.728$ shows a strong [CII] line with an integrated flux density of 5.40 ± 0.24 Jy km s^{-1}, which is consistent within the errors to the value of 4.79 ± 0.38 Jy km s^{-1} found for this source by

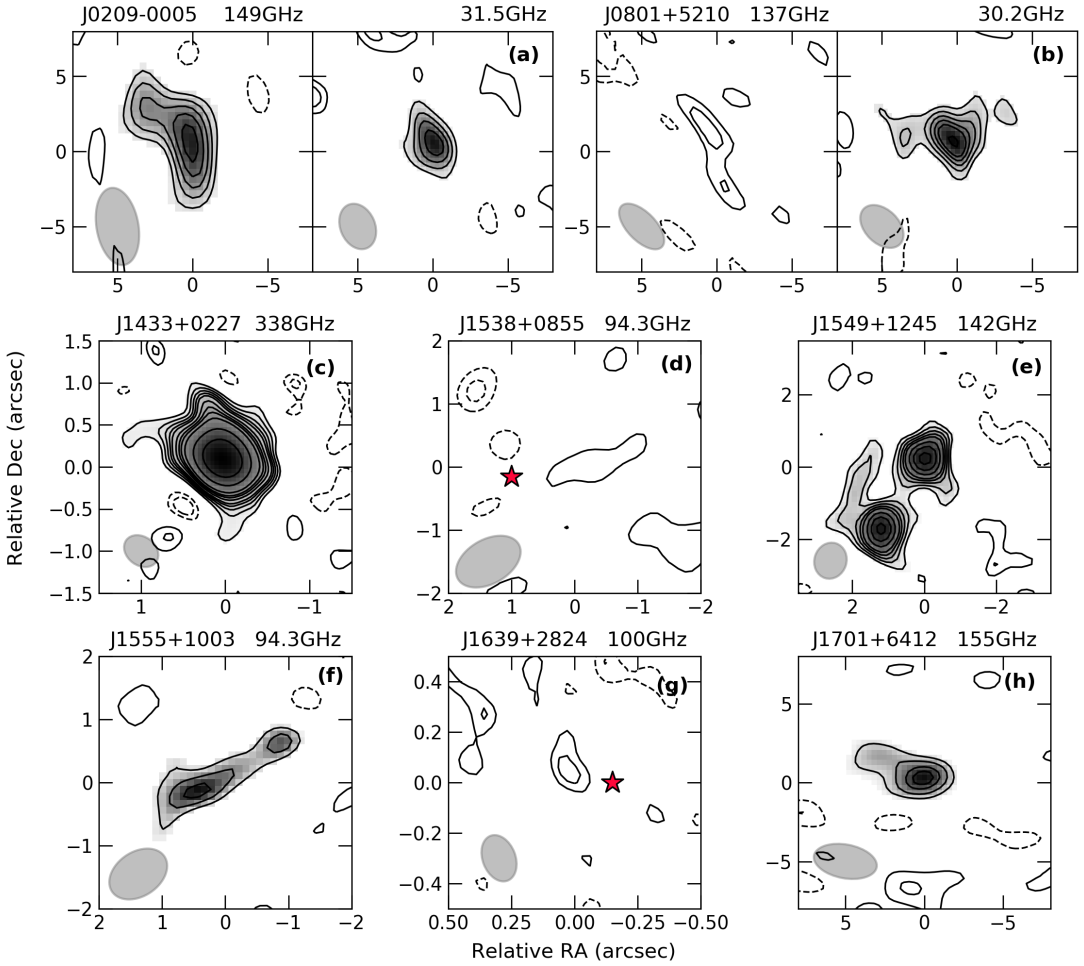

Fig. 2. Maps of the continuum emission for the WISSH QSOs analysed in this work. For each panel, the observed continuum frequency is indicated by the top label. Grayscale defines the region where emission from the QSO host-galaxy and nearby continuum emitters is detected with $S/N \gtrsim 4.5$. Black contours correspond to $[-3, -2, 2, 3, 4, 5, 6, 8, 12, 16, 32, \ldots]\sigma_{\rm cont}$, where $\sigma_{\rm cont}$ values are listed in Table 1. Dashed contours are for negative values. The beam of each observation is also shown by the grey ellipse. *Panels d* and *g*: the red star indicates the QSO optical position from SDSS.

Nguyen et al. (2020) for the same observation. [CII] emission in J1433+0227 is a factor of ∼10 brighter than what found in the WISSH QSO J1015+0020 at $z_{\rm cold} \sim 4.4$, also targeted in [CII] by Bischetti et al. (2018). This result is consistent with the variety of [CII] properties typically observed in high-z QSOs (e.g. Trakhtenbrot et al. 2017; Nguyen et al. 2020). [CII] emission in J1433+0227 is spatially resolved, with a deconvolved size of $(0.44 \pm 0.03) \times (0.38 \pm 0.03)$ arcsec^2, corresponding to $\sim 2.9 \times 2.5$ kpc^2. A second weak (peak flux density ∼1 mJy) [CII] emitter has been detected at a distance of 12 kpc (Fig. 3c), showing an almost null velocity shift of 60 ± 40 km s^{-1} with respect to the QSO redshift.

J1538+0855. We have detected CO(4−3) emission with a modest significance of $\sim 4.5\sigma_{\rm CO}$ from the host-galaxy of this QSO, located at $z_{\rm cold} \sim 3.572$. The peak of CO emission is separated by ∼1 arcsec from the SDSS optical position of the QSO, the offset being comparable to the uncertainty on the SDSS position. The line profile has a peak flux density of ∼1 mJy and a FWHM of 400 ± 40 km s^{-1}. No additional sources have been detected in the ALMA maps.

J1549+1245. CO(4−3) emission in this QSO is characterised by a narrow line profile, with a $FWHM = 245 \pm 50$ km s^{-1}, and a peak flux density of ∼1 mJy. Despite the modest resolution of ALMA observations (1 arcsec), CO emission is resolved and has a deconvolved size of $(1.10 \pm 0.16) \times (0.86 \pm 0.16)$ arcsec^2. Indeed, J1549+1245 is a peculiar case, showing two line emitting sources within a small separation of ∼2.4 arcsec (Fig. 3e). The strongest one, located at ∼19 kpc south-east of the nucleus, shows CO(4−3) emission as bright as that of the QSO, with a deconvolved size of $(1.24 \pm 0.15) \times (0.55 \pm 0.13)$ arcsec^2. Such emission is blue-shifted by ∼950 km s^{-1} with respect to the redshift of J1549+1245 and shows a $FWHM \sim 540$ km s^{-1}. A second, fainter CO(4−3) emitting companion is also observed ∼12 kpc north of the QSO, with a modest velocity shift of 200 ± 40 km s^{-1}.

J1555+1003. This QSO shows a broad ($FWHM = 615 \pm 90$ km s^{-1}) CO(4−3) emission line profile peaking at ∼1.4 mJy, located at $z_{\rm cold} \sim 3.529$. The resolution of our ALMA observations has allowed us to marginally resolve CO(4−3) emission produced by a nearby companion galaxy, distant only 6 kpc from the QSO in the west direction (Fig. 3f).

J1639+2824. For this QSO, we measure a CO(4−3) based redshift $z_{\rm cold} = 3.846 \pm 0.001$, significantly larger than the redshift $z = 3.840$ derived from the same data by Schramm et al. (2019). However, we note that the latter would correspond to an observed $\nu_{\rm obs} \sim 95.37$ GHz, inconsistent with the CO(4−3)

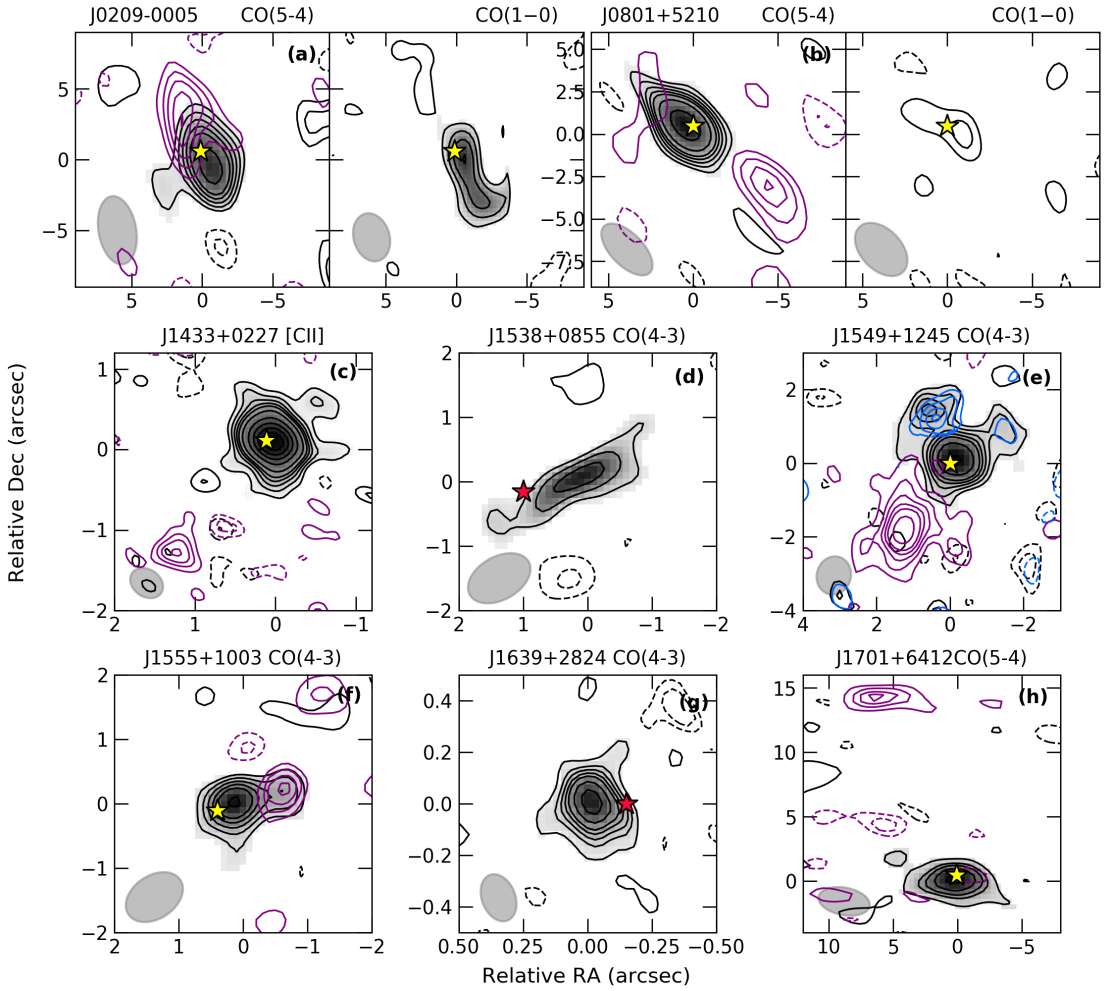

Fig. 3. Maps of the cold gas emission for the WISSH QSOs analysed in this work, obtained by integrating over the spectral range covered by CO or [CII] emission. For each source, the targeted transition is indicated by the top label. Grayscale defines the region where line emission from the QSO host-galaxy is detected with $S/N \gtrsim 4.5$. Black contours correspond to $[-3, -2, 2, 3, 4, 5, 6, 8, 12, 16, 32, \ldots]\sigma_{\rm cold}$ in the QSO map, where $\sigma_{\rm cold} = 0.16, 0.012\,{\rm Jy\,beam^{-1}\,km\,s^{-1}}$ for CO(5–4) and CO(1–0) observations in *panel a* and $0.22, 0.032\,{\rm Jy\,beam^{-1}\,km\,s^{-1}}$ in *panel b*. *Panels c–h*: $\sigma_{\rm cold} = 0.091, 0.098, 0.021, 0.11, 0.082, 0.18\,{\rm Jy\,beam^{-1}\,km\,s^{-1}}$, respectively. Similarly, magenta and blue contours identify emission from companion line emitters. *Panel e*: blue contours have been created by masking QSO emission in a circular aperture of 1 arcsec radius centred on the QSO location. Dashed contours are for negative values. Yellow (red) stars indicate the QSO position as traced by the millimetre (optical) continuum. The beam of each observation is also shown by the grey ellipse.

spectrum shown in their Fig. 3. The CO(4−3) emission line profile has a $FWHM = 615 \pm 90\,{\rm km\,s^{-1}}$, and an integrated flux density of $\sim$0.9 Jy km s^{-1}. By fitting a 2D elliptical Gaussian to the data (in the image and *uv* plane), we measure an emission size of $(0.15 \pm 0.02) \times (0.11 \pm 0.02)\,{\rm arcsec^2}$ (Fig. 3g). We note that our measured minor axis is a factor of about two larger than the value reported by Schramm et al. (2019), likely due to the larger velocity range that we used to produce the velocity-integrated CO(4−3) map (solid histogram in Fig. 4g), compared to Schramm et al. (2019), who reported a $FWHM = 495 \pm 30\,{\rm km\,s^{-1}}$. No additional sources have been detected in the ALMA maps.

J1701+6412. We have detected CO(5−4) emission from this QSO, associated with a $z_{\rm cold} = 2.753$. Similarly to the other CO(5−4) targets in our sample, the line peaks at >2 mJy, with an associated integrated flux density of $1.5 \pm 0.35\,{\rm Jy\,km\,s^{-1}}$. In the NOEMA maps we have detected a companion galaxy distant $\sim$130 kpc from J1701+6412, showing CO(5−4) blue-shifted (by $\sim$1800 km s^{-1}) emission, whose flux is about one third of that of the QSO.

For each target and for the companion galaxies, we compute CO or [CII] luminosity according to Eqs. (1) and (3) in Solomon & Vanden Bout (2005), respectively. The resulting CO luminosities, listed in Table 2, are in the range $L'_{\rm CO} \sim (0.5–7) \times 10^{10}\,{\rm K\,km\,s^{-1}\,pc^2}$ for the QSO host galaxies. For the companion galaxies, we measure $L'_{\rm CO}$ in the range $(0.1–1.7) \times 10^{10}\,{\rm K\,km\,s^{-1}\,pc^2}$. The CO luminosity of the companion is typically a factor of $\sim$3–5 lower or, in the case of J0209–0005 and J1549+1245, comparable to that of the QSO host. In the case of J1433+0227, we measure a [CII] luminosity $L_{\rm [CII]} = (3.72 \pm 0.16) \times 10^9\,L_\odot$.

3.3. Investigating the CO spectral line energy distribution

As mentioned in Sect. 3.2, J0209–0005 and J0801+5210 have been observed in both CO(5−4) and CO(1−0) rotational transitions. It is therefore possible to derive some information on the excitation conditions of the gas in WISSH QSOs from the relative strength of these two lines. In the case of J0209–0005, we measure a ratio of the integrated flux densities

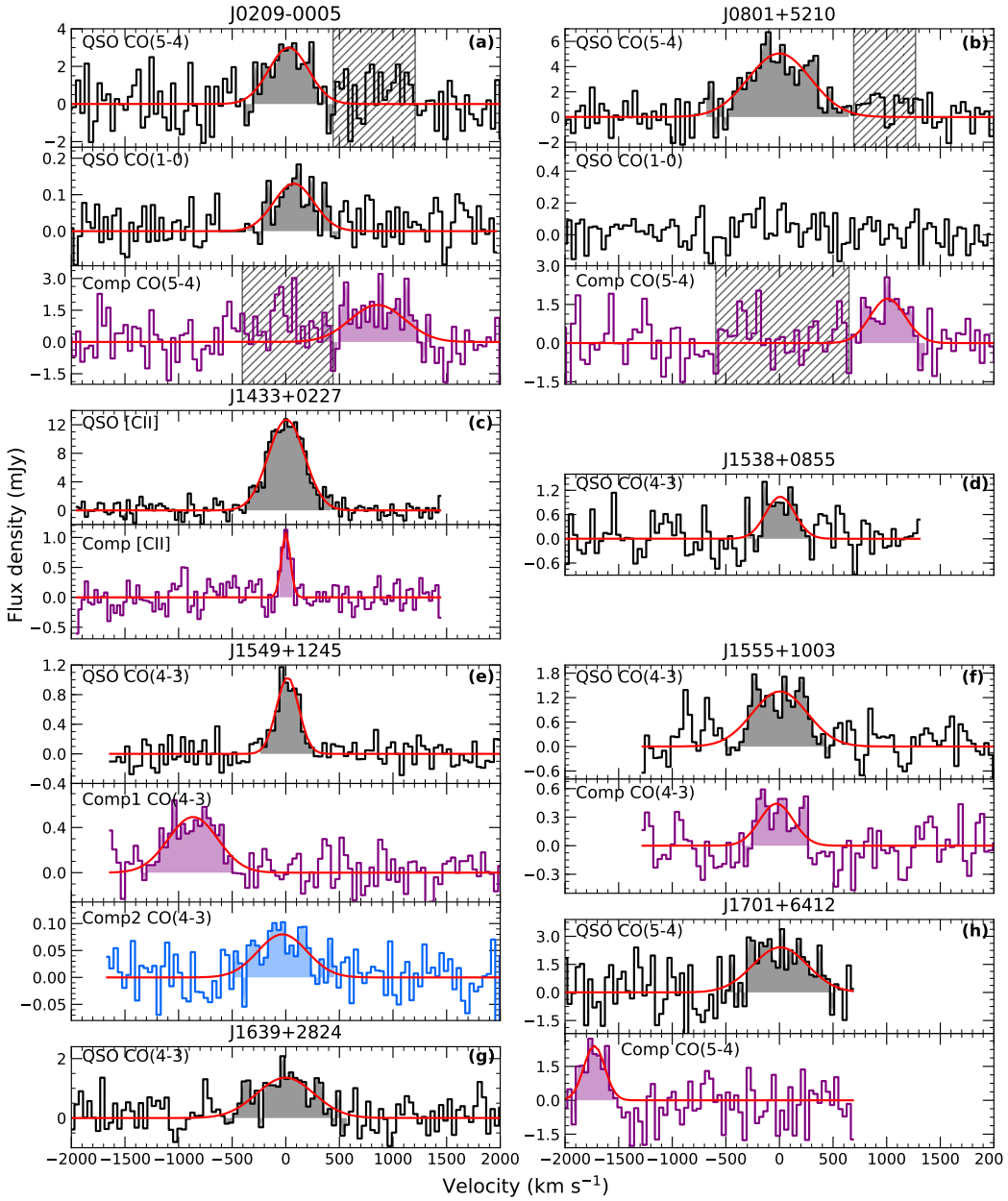

Fig. 4. Spectra of the CO or [CII] emission lines for the WISSH QSOs analysed in this work. For each source, the targeted transition is indicated by the top label. Spectra were extracted from the region where emission from the QSO host-galaxy is detected with $S/N > 2$ (see Fig. 3) and show the velocity range $v \in [-2000, +2000]$ km s^{-1} in channels of 40 km s^{-1}. In case of (e), we preferred a circular extraction region with size of the ALMA beam, centred on the QSO position, to limit contamination from a nearby line emitting source at 0.6 arcsec separation (see Fig. 3e). The best-fit, Gaussian profiles are shown by the red curve. The filled histogram indicates velocity channels in which emission in the QSO and companion spectra is >5% than the peak flux of the best-fit model. *Panels a* and *b*: grey spectral regions were excluded from the fit because associated with line emission from nearby sources (see Sect. 3.2) partially unresolved by the NOEMA beam.

$S\Delta v_{5-4}/S\Delta v_{1-0} = 22.5 \pm 6.0$, while for J0801+5210 we infer the lower limit $S\Delta v_{5-4}/S\Delta v_{1-0} > 36.0$. Figure 5 shows the CO SLED of J0209–0005 and J0801+5210, compared to few QSOs from literature with accurate measure of CO transitions up to $J \gtrsim 5$ (Carilli & Walter 2013). We also include the $z \sim 2.5$ reddened QSO ULAS J1234+0907 from Banerji et al. (2018). We note that the $S\Delta v_{5-4}/S\Delta v_{1-0}$ ratio measured for J0209–0005 is similar to the values reported in other QSOs, while that of J0801+5210 suggests that CO can be highly excited in our hyper-luminous QSOs (see Sect. 6.3 for further discussion).

By translating CO flux ratios in CO luminosity ratios, we obtain $L'_{\rm CO(5-4)}/L'_{\rm CO(1-0)} = 0.90 \pm 0.24$ and $L'_{\rm CO(5-4)}/L'_{\rm CO(1-0)} >$ 1.39 for J0209–0005 and J0801+5210, respectively. The ratio measured for J0209–0005, based on the detection of both CO(1−0) and CO(5−4), is consistent within the uncertainty with the typical luminosity ratio reported for QSO host galaxies by Carilli & Walter (2013). We thus adopt $L'_{\rm CO(5-4)}/L'_{\rm CO(1-0)} \simeq 0.69$ and $L'_{\rm CO(4-3)}/L'_{\rm CO(1-0)} \simeq 0.87$ (Carilli & Walter 2013) to infer CO(1−0) luminosity in the remaining WISSH QSOs from the observed mid-J CO rotational transitions. We note that by assuming the CO SLED of J0209–0005, the inferred $L'_{\rm CO(1-0)}$ would be lower by a factor of $\gtrsim$2. On the other hand, by considering the CO ladder of the Cloverleaf QSO (Riechers et al. 2011a), which shows the minimum measured CO(5−4)/CO(1−0) ratio

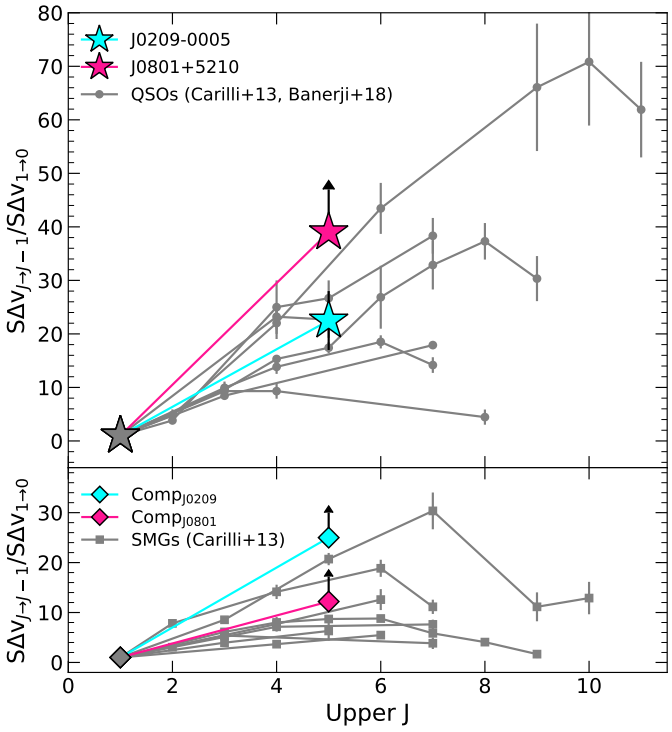

Fig. 5. *Top panel*: CO SLED of J0209–0005 and J0801+5210 with CO(1−0) and CO(5−4) observations, compared to QSOs from literature with available measure of the ground transition (Carilli & Walter 2013). *Bottom panel*: CO ladder of companion galaxies Comp$_{J0209}$ and Comp$_{J0801}$, together with CO SLEDs of SMGs.

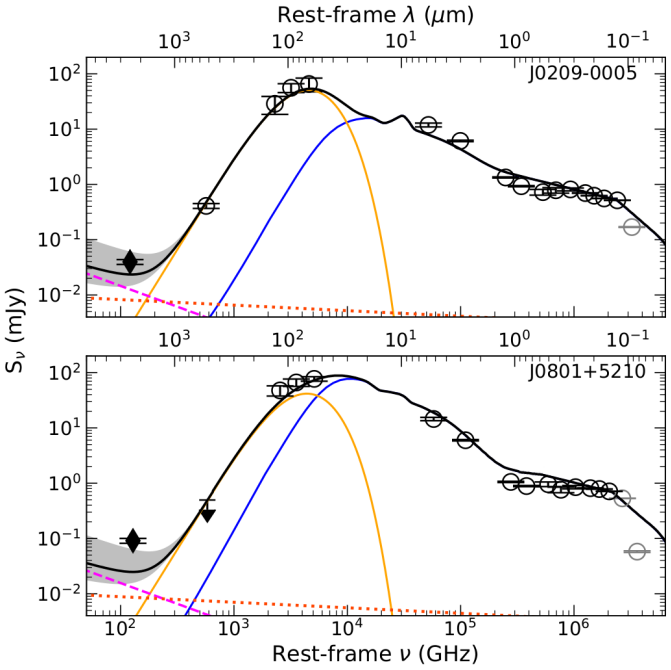

Fig. 6. Rest-frame SED of J0209–0005 (*top*) and J0801+5210 (*bottom*). In each panel, black circles indicate the photometric points considered (arrows represent 3σ upper limits). Photometric points at $\lambda < 1216$ Å are not included in the fits due to Lyα absorption (grey circles). Rest-frame 125 GHz continuum data (not included in the fit) are shown by diamonds. Black curve represents the total best fit model, while blue(orange) curve refers to the QSO(cold dust) emission component. Synchrotron and free free emission are shown by the dashed and dotted lines, respectively.

in Fig. 5, the inferred $L'_{CO(1-0)}$ would be higher by a factor of ∼1.3.

Finally, the CO(5−4) and CO(1−0) observations also probe molecular gas excitation in the companion galaxies around J0209–0005 and J0801+5210 (see Sect. 3.2). The lower limits inferred for the integrated CO(5−4)/CO(1−0) flux ratios in Comp$_{J0209}$ and Comp$_{J0801}$ are shown in the bottom panel of Fig. 5, compared with CO SLEDs of sub-millimetre galaxies (SMGs) from literature (Carilli & Walter 2013). The $S\Delta v_{5-4}/S\Delta v_{1-0} > 25$ measured in Comp$_{J0209}$ indicates a high CO excitation, similar to the excitation in the QSO host-galaxy, while in Comp$_{J0801}$ we found $S\Delta v_{5-4}/S\Delta v_{1-0} > 12$, consistent with the typical CO SLED of SMGs (e.g. Casey et al. 2014).

4. Broad band SEDs and millimetre emission

The observations presented in Sect. 3.1 have provided us with a measure of the rest-frame 430−1935 GHz continuum, which can be used to extend to (sub-)millimetre wavelengths the coverage of the spectral energy distribution (SED) presented in Duras et al. (2017) for the half of our sample with available *Herschel* photometry. For QSOs with no *Herschel* coverage, we combine ALMA and NOEMA continuum measurements with the average infrared properties of WISSH-*Herschel* QSOs to provide an estimate of L_{IR}. We complement sub-mm data with archival SDSS DR12 (Alam et al. 2015), 2MASS (Skrutskie et al. 2006), WISE (Wright et al. 2010), and *Herschel*/SPIRE (Pilbratt et al. 2010; Griffin et al. 2010) broad-band photometry. For target J1555+1003, undetected by 2MASS, we include photometric points obtained from dedicated observations at the ESO-INAF Rapid Eye Mount (REM) telescope (P.I. M. Bischetti) and INAF Telescopio Nazionale *Galileo* (TNG, P.I. V. Testa). These observations provided us with magnitudes $J = 17.4 \pm 0.11$, $H = 16.47 \pm 0.12$ and $K' = 16.16 \pm 0.13$ for J1555+1003.

ALMA has revealed the presence of a strong continuum emitter close to J1549+1245 (Fig. 2). QSO and companion being separated by ∼2.4 arcsec, cannot be resolved as distinct objects in the WISE images, given the PSF, which is in the range 6.1−12 arcsec. However, we have verified that emission is centred at the QSO location in all WISE bands and estimated the companion contamination, as traced by irregular morphology of the WISE contours, to be <10%. Moreover, the J1549+1245 companion is undetected in one hour exposure VLT/SINFONI H and K band observations of the SUPER ESO large program 196.A-0377 (P.I. V. Mainieri, Circosta et al. 2018; Kakkad et al. 2020). An upper limit of $S_{cont} < 0.54$ mJy on the QSO continuum emission at ∼785 GHz inferred from ACA observations has also been included in the SED (Fig. A.1).

In the case of J0209–0005, the continuum emission associated with the companion galaxy is ∼25−35% of the QSO continuum in the NOEMA band (Fig. 2a). To compute the SED of J0209–0005, we assume *Herschel* photometry to be similarly dominated by emission from the QSO host-galaxy.

SED Fitting was performed by using the procedure presented in Duras et al. (2017), Zappacosta et al. (2018) with a combination of QSO and host-galaxy emission components. In summary, the QSO component is described as the superposition of accretion disk emission (Feltre et al. 2012), and of radiation coming from a clumpy, two-phase dusty torus (Stalevski et al. 2016). Cold dust emission is modelled as a non-approximated modified

Table 3. Properties of the ISM and molecular gas reservoir in the host-galaxies of WISSH QSOs.

ID	$\log L_{\rm IR}$ ($L_\odot$)	SFR ($M_\odot\,{\rm yr}^{-1}$)	SFE ($L_\odot$/(K km s^{-1} pc^2))	$\log M_{\rm dust}$ ($M_\odot$)	$\log M_{\rm gas}$ ($M_\odot$)	$M_{\rm gas}/M_{\rm dust}$	$\tau_{\rm dep}$ (Myr)
(1)	(2)	(3)	(4)	(5)	(6)	(7)	(8)
J0209–0005	13.17	735 [465–1165]	310 [230–415]	8.14	10.28 ± 0.08	140	25 [15–40]
J0801+5210	13.24	875 [550–1385]	195 [150–250]	8.22	10.55 ± 0.04	210	40 [25–65]
J1433+0227	12.74	270 [170–430]	–	8.74	11.00 ± 0.30 [(b)]	180 [(a)]	360 [180–700]
J1538+0855	12.82	330 [165–660]	235 [120–470]	8.04	10.05 ± 0.12	100	35 [15–65]
J1549+1245	12.52	165 [85–330]	305 [155–610]	7.64	9.64 ± 0.04	100	25 [15–50]
J1555+1003	12.94	435 [220–870]	130 [65–260]	8.01	10.43 ± 0.09	260	60 [30–120]
J1639+2824	12.72	260 [130–520]	65 [35–130]	8.04	10.51 ± 0.07	300	125 [55–245]
J1701+6412	13.34	1095 [690–1735]	460 [340–625]	8.14	10.28 ± 0.09	140	15 [10–25]
J1015+0020 [(*)]	12.11	100 [65–160]	–	7.02	9.28 ± 0.30 [(b)]	180 [(a)]	20 [10–45]

Notes. Columns give the following information: (1) SDSS ID, (2) SED-based infrared luminosity (see Sect. 4) in the range $\lambda = 8-1000\,\mu$m. Typical uncertainty on $L_{\rm IR}$ is 0.1 dex for sources with *Herschel* photometry, while for the other QSOs we consider a 0.3 dex error. (3)–(4) AGN-corrected SFR and star-formation efficiency, (5) Dust mass, (6) Molecular gas mass, (7) Gas-to-dust ratio, and (8) Molecular gas depletion time. In the last row we report the same quantities measured for J1015+0020, a WISSH QSO presented in Bischetti et al. (2018). [(*)]Presented in Bischetti et al. (2018). [(a)]Average value measured from WISSH QSOs with CO-based $M_{\rm gas}$. [(b)]Computed assuming $M_{\rm gas}/M_{\rm dust} = 180$.

blackbody that accounts for emission powered by star formation, absorbed and then re-emitted by the surrounding dust at mid- and far-infrared wavelengths. We use a library of 70 modified black-body templates covering the temperature range from 30 to 100 K, and we assume a power-law dependence of the optical depth with wavelength, that is $\tau_\lambda \propto \lambda^\beta$, where $\beta = 1.6$ is the dust emissivity index typically used in high-z QSOs (e.g. Beelen et al. 2006). Dust temperature is a free parameter for all sources with *Herschel* photometry, while for the remaining sources we assume $T_{\rm dust} = 60$ K, i.e. the average measured temperature for the total sample of 16 WISSH-*Herschel* QSOs (Duras et al. 2017). We note that assuming a $T_{\rm dust} = 40(80)$ K would result in a 50% lower(a factor of two higher) $L_{\rm IR}$.

Figure 6 shows the resulting rest-frame UV to far-infrared SEDs for J0209–0005 and J0801+5210, while the SEDs of the other WISSH QSOs are shown in Appendix A. For all sources, the SED is dominated by the QSO component (blue curve) at all wavelengths below several tens of μm. By integrating the QSO component in the range $1-1000\,\mu$m we infer intrinsic QSO bolometric luminosities in the range $L_{\rm Bol} \sim 3.6 \times 10^{47}-1.0 \times 10^{48}$ erg s^{-1}. Concerning emission from cold-dust in the QSO host-galaxies (orange curve), we measure large values of the infrared, $8-1000\,\mu$m integrated luminosity in our targets, that is $L_{\rm IR} \simeq (1.7-8.3) \times 10^{46}$ erg s^{-1} (Table 3). However, some authors (e.g. Symeonidis 2017; Kirkpatrick et al. 2019) argued that a significant fraction of the infrared emission in luminous AGN might be due to dust heated by the large radiative output of the accreting SMBH up to kpc scale. In particular, the amount of AGN-heated dust in the WISSH-*Herschel* QSOs was estimated through radiative transfer by Duras et al. (2017), who found an average AGN contribution to $L_{\rm IR}$ of 50% at $L_{\rm Bol} > 10^{47}$ erg s^{-1}. Accordingly, we compute the AGN-corrected infrared luminosities of our WISSH QSOs by dividing by a factor of two the values listed in Table 3. Therefore, from these corrected values we derive the SFR using the relation by Kennicutt (1998) scaled to a Chabrier initial mass function.

In Fig. 6, the rest-frame ~125 GHz continuum of J0209–0005 and J0801+5210 is shown (solid diamonds). These JVLA photometric points were not included in the fitting because non-thermal and thermal bremsstrahlung emission significantly contribute to the SED at these frequencies, in addition to dust emission. Disentangling the relative contribution of these processes is not feasible without several photometric points at $\nu < 200$ GHz. However, it is possible to estimate the AGN contribution at these frequencies by comparing the observed JVLA fluxes with typical emission from star forming galaxies. Specifically, we use the (AGN-corrected) SFR derived from SED fitting to compute the synchrotron and free free energy distribution (dashed and dotted lines in Fig. 6) according to Eqs. (12) and (13) by Yun & Carilli (2002), respectively. The gray shaded area indicates the scatter of non-thermal emission observed in local starburst galaxies for a given SFR (Yun & Carilli 2002). In the case of J0209–0005, the ~125 GHz continuum is consistent with no AGN contribution, while in J0801+5210 the QSO continuum shows a small excess (by factor of 1.5) with respect to the values found in the starburst case. This may suggest a small but non negligible contribution of the AGN to mm-radio wavelengths. The extrapolation at radio wavelengths of the synchrotron and free free SED of both J0209–0005 and J0801+5210 is consistent with the non detections at 1.4 GHz in the VLA Faint Images of the Radio Sky at Twenty-Centimeters (FIRST) survey (Helfand et al. 2015).

By exploiting the relation between the infrared continuum emission and the cold-dust mass, we derive an estimate of the dust content in the host-galaxy of the WISSH QSOs as follows (e.g. Beelen et al. 2006; Scoville et al. 2016)

$$M_{\rm dust} = \frac{S_\lambda D_{\rm L}^2}{k_{\rm dust} B(\lambda, T_{\rm dust})}, \quad (1)$$

where S_λ is the continuum flux density at rest-frame $\lambda = 850\,\mu$m, measured from the best-fit SED model, $D_{\rm L}$ is the luminosity distance, $k_{\rm dust} = 0.077$ kg^{-1} m^2 is the dust mass opacity at $850\,\mu$m (Dunne et al. 2000) and $B(\lambda, T_{\rm dust})$ is the Planck function for a given dust temperature. The latter is also based on our SED fitting, in the range $T_{\rm dust} \in [40, 75]$ K. The resulting $M_{\rm dust}$ are listed in Table 3.

5. CO and [CII] kinematics

We analyse here the CO and [CII] kinematics of the three WISSH QSOs with spatially resolved emission, for which it has been possible to investigate the presence of gradients in the velocity (Moment 1) and velocity dispersion (Moment 2) maps.

Figure 7a shows the velocity map associated with [CII] emission in J1433+0227. A velocity gradient is detected in

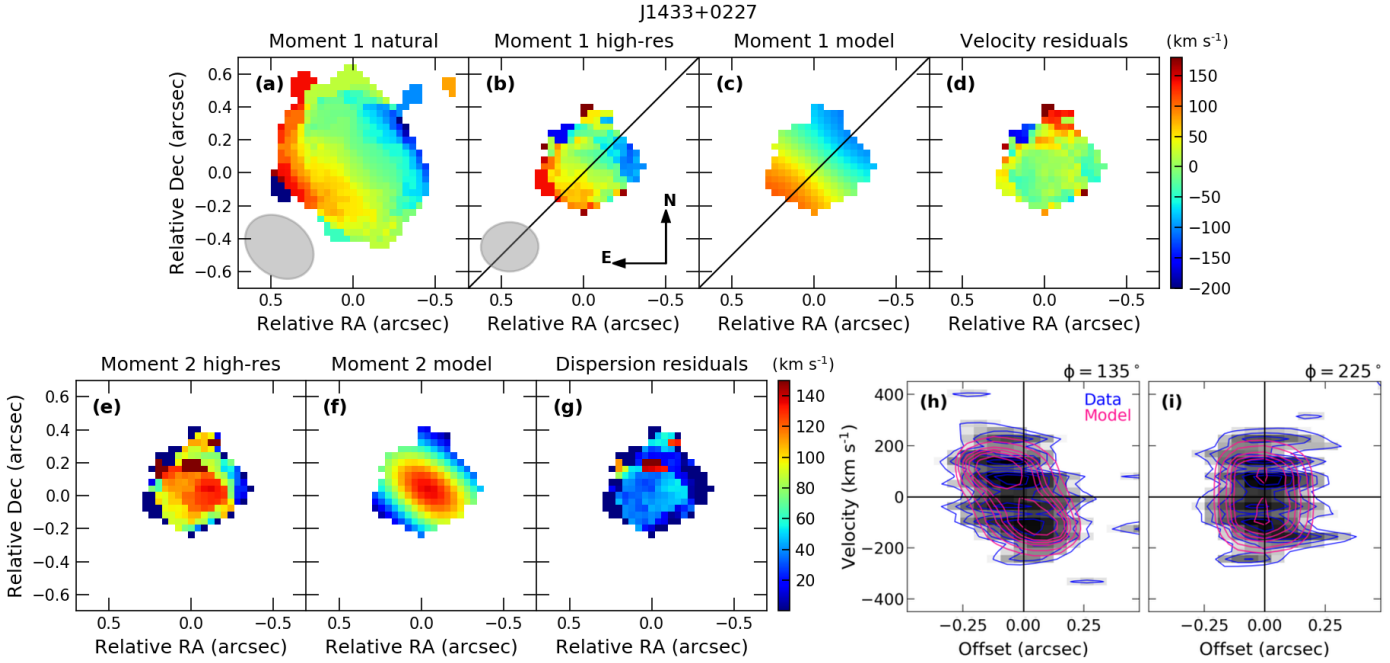

Fig. 7. Velocity maps of J1433+0227 associated with CO(4–3) emission detected at $>3\sigma_{40\,\mathrm{km\,s^{-1}}}$ significance in the original (*a*) and high-resolution (*b*) maps, in which $\sigma_{40\,\mathrm{km\,s^{-1}}} = 0.43$ mJy beam^{-1} and 0.71 mJy beam^{-1}, respectively. ALMA beams are shown by the grey ellipses. *Panel c*: velocity map for the best-fit BAROLO model of a rotating disk. Black line indicates the major kinematic axis of the model. Velocity residuals are shown in *panel d*. *Panels e–g*: velocity dispersion maps associated with the high-resolution ALMA data and the best-fit BAROLO model, and the dispersion residual map. Position-velocity diagram associated with the high-resolution datacube along major (*h*) and minor (*i*) kinematic axes are also shown. Top labels indicate the associated position angles (measured anti-clockwise from north). Blue contours refer to the $[2,3,4,5,6,8,\ldots]\sigma_{40\,\mathrm{km\,s^{-1}}}$ significance.

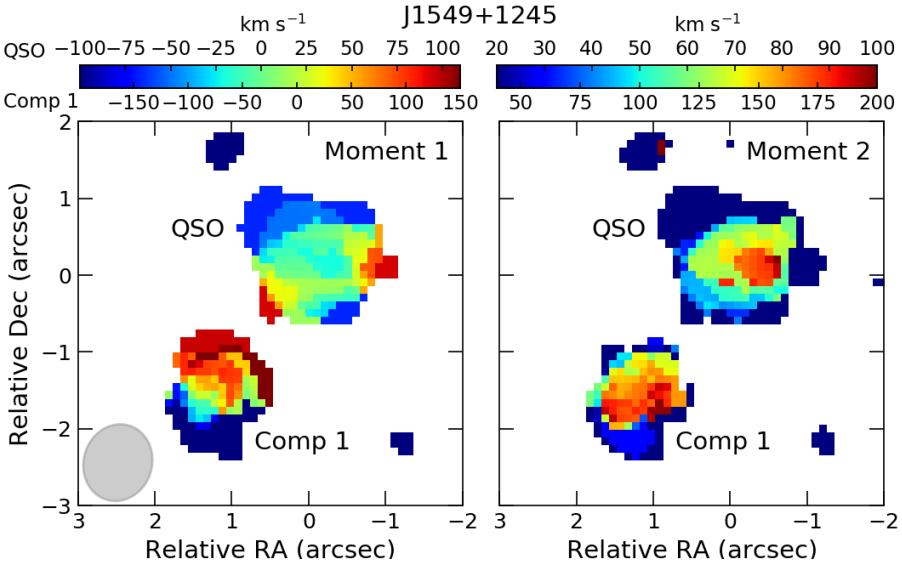

Fig. 8. Velocity (*left*) and velocity dispersion (*right*) maps of J1549+1245 and its bright companion, associated with CO(4–3) emission detected at $>3\sigma$ significance. In both panels, *top* (*bottom*) colorbar labels indicate values observed in the QSO (companion). The ALMA beam is also shown by the grey ellipse.

approximately the north-west to south-east direction, with a projected velocity in the range $v \in [-100, +130]$ km s^{-1}, although the gradient associated with emission in the inner 0.5 arcsec around the nucleus shows a different orientation than emission at larger angular separation. Perturbations are present in the north direction, where emission with $v \sim 0$ km s^{-1} smears out the gradient. We have fitted the 3D-BAROLO tilted-ring model (Di Teodoro & Fraternali 2015) to the data to provide a description of the kinematics. However, the combination of disturbed morphology and limited angular resolution (0.44×0.34 arcsec^2) hampers an accurate estimate of the source inclination and, in turn, of the kinematical properties. We have thus produced an ALMA [CII] datacube with increased angular resolution by applying a Briggs weighting of the visibilities with robust parameter $b = -0.5$ (Briggs 1995), resulting in a beamsize of 0.35×0.30 arcsec^2 (Fig. 7b). The associated position-velocity diagram of the [CII] emission detected above 3σ ($\sigma_{40\,\mathrm{km\,s^{-1}}} = 0.71$ mJy beam^{-1}) is also shown in Figs. 7h and i.

The 3D-BAROLO fit of the high-resolution datacube results into an inclination $i = 34 \pm 10$ deg, which is consistent with that derived from the projected axes ratio of the CO emission measured in Sect. 3.2 and the $i \sim 39$ deg reported by

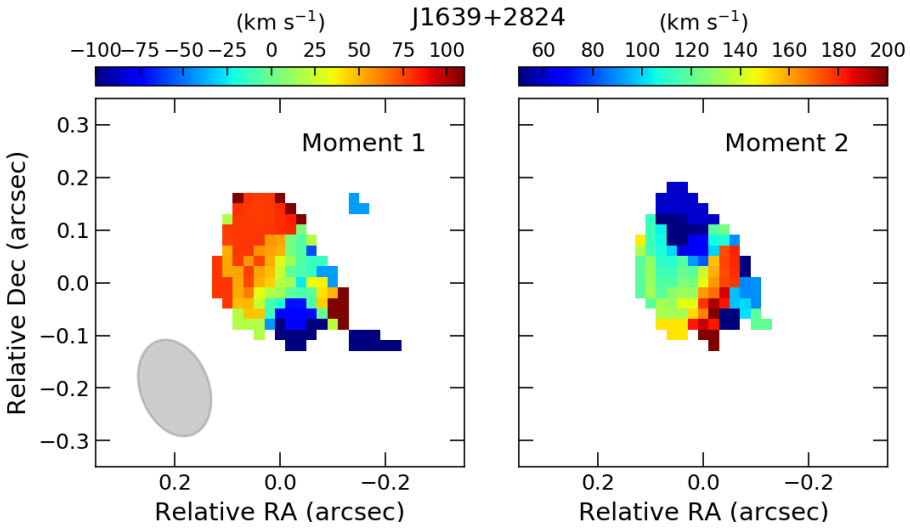

Fig. 9. Velocity (*left*) and velocity dispersion (*right*) maps of J1639+2824, associated with CO(4−3) emission detected at >3σ significance. The ALMA beam is also shown by the grey ellipse.

Nguyen et al. (2020). The velocity residuals map (Fig. 7d) globally shows small deviations comparable to the spectral resolution, except for the northern region, where blue- and red-shifted residuals up to $|v| \sim 150\,\mathrm{km\,s^{-1}}$ can be observed. Residuals in correspondence of the northern region are also visible in the dispersion residuals map (Fig. 7g). Similarly, the overlay of data and BAROLO contours in the position-velocity diagram indicates that the bulk of the [CII] emission in J1433+0227 is compatible with a rotating disk, although deviations from pure rotation are visible along both major and minor kinematic axes. We infer an intrinsic circular velocity $v_{\rm circ} = 1.3{\times}\Delta v_{\rm blue-red}/(2\sin i) \simeq 400\,\mathrm{km\,s^{-1}}$ (e.g. Förster Schreiber et al. 2009; Tacconi et al. 2013; Bischetti et al. 2019a), where $\Delta v_{\rm blue-red} \simeq 350\,\mathrm{km\,s^{-1}}$ is the total velocity gradient measured from contours of BAROLO model at ∼5σ in the position-velocity diagram at a projected distance of ∼1.2 kpc from the nucleus.

Figure 8 reports the velocity and velocity dispersion maps associated with CO(4−3) emission in the WISSH QSO J1549+1245. At the resolution of ∼1 arcsec^2, we do not identify a clear velocity gradient, the bulk of the emission showing a flat velocity profile with $|v| < 50\,\mathrm{km\,s^{-1}}$. Structures with blue-shifted ($v \sim -150\,\mathrm{km\,s^{-1}}$) and red-shifted ($v \sim +100\,\mathrm{km\,s^{-1}}$) velocity are observed only in the outer region. The J1549+1245 velocity profile is consistent with the low inclination $i \sim 40$ deg derived from the projected axes ratio. The velocity dispersion map shows a peak dispersion value of $\sim$100 km s^{-1} about 0.5 arcsec offset from the QSO position in the west direction, which may be related to disturbed kinematics. Given the $S/N \sim 16$ of the CO emission, increasing the angular resolution by Briggs weighting the visibilities does not provide further information on the J1549+1245 kinematics. Figure 8 also shows the moment maps of the bright companion south-east of J1549+1245, namely Comp1$_{\rm J1549}$. This source shows a large velocity gradient with $v \in [-200, +150]\,\mathrm{km\,s^{-1}}$, approximately in the south-east to north-west direction. Such gradient may be interpreted as the bulk of CO(4−3) in Comp1 originating from an inclined ($i \sim 64$ deg) rotating disk, although the limited S/N and resolution do not allow us to fit a disk model to the data. The velocity dispersion map displays large values up to $\sigma \sim 200\,\mathrm{km\,s^{-1}}$ at the position of Comp1 and in the direction of J1549+1245.

Although the modest SNR of the CO(4−3) emission prevents us from performing a BAROLO fit of the data, the velocity map of J1639+2824 (Fig. 9) appears similar to that of J1433+0227. Indeed, a velocity gradient is detected in the north-east to south-west direction, with projected velocity range $v \in [-100, +100]\,\mathrm{km\,s^{-1}}$, smeared out at ∼[−0.1, −0.05] arcsec by some disturbances. The presence of perturbed motions is also supported by the high velocity dispersion of the gas in the same region, where $\sigma \sim 150$−$200\,\mathrm{km\,s^{-1}}$.

We point out that, in the case of marginally resolved targets observed with modest significance, such as J1549+1245 and J1639+2824, the interpretation of moment maps is not straightforward and can be affected by large uncertainties. As an example, non-rotating ISM components such as outflows and merger-induced perturbations may be mixed with rotation and affect the observed velocity gradients (e.g. Díaz-Santos et al. 2016; Trakhtenbrot et al. 2017; Bischetti et al. 2019a). Moreover, velocity dispersion profiles in the central regions may be affected by beam-smearing effects (e.g. Davies et al. 2011; Tacconi et al. 2013). Higher angular resolution of these QSOs are needed to properly map the cold gas kinematics in their host galaxies.

6. Discussion

6.1. The rich environment of hyper-luminous QSOs

In a pilot study targeting [CII] emission around the WISSH QSO J1015+0020, Bischetti et al. (2018) found a large galaxy overdensity with three [CII] emitters at close distance (∼2−16 kpc) and two continuum emitters likely physically associated. In this work we build on the Bischetti et al. (2018) result by testing the role of luminous QSOs as signposts of large galaxy overdensities in a fair statistical sample.

We confirm that QSOs at the brightest end of the luminosity function with $L_{\rm Bol} > 10^{47}\,\mathrm{erg\,s^{-1}}$ pinpoint high density regions, as we find that ∼75% (80%, once J1015+0020 is included) of WISSH sources show at least one companion sub-millimetre galaxy. Specifically, six out of eight QSOs analysed here have a nearby line emitter, showing bright CO or [CII] emission at about the same redshift and in most cases of comparable luminosity to that of the QSO host-galaxy. These emitters are generally located at close distance (∼6−40 kpc) from the QSO, with the exception of Comp$_{\rm J0209}$ which is located further away (∼130 kpc). Two of them, namely Comp$_{\rm J0209}$ and Comp1$_{\rm J1549}$, are detected also in continuum emission, with a flux which is ∼30−100% that of the QSO. This suggests that a significant fraction of the SFR in the observed QSO-companion systems takes

place in the companion galaxies, similarly to Bischetti et al. (2018) findings and in agreement with expectations from semi-analytical models (e.g. Fogasy et al. 2017).

Our results provide useful observational evidence to the hotly debated issue of whether high-redshift QSOs reside in overdense regions. Traditional studies of QSO environment mainly rely on HST imaging in the UV and optical bands. In the case of dust-reddened or Type 2 QSOs, a large fraction (∼50−80%) have been found to reside in interacting systems (Urrutia et al. 2008; Glikman et al. 2015; Wylezalek et al. 2016; Fan et al. 2016). However, in Type 1 sources such as WISSH QSOs, the overshining nuclear emission complicates the detection of tidal features and close/minor mergers, leading to conflicting results about the fraction of interacting systems (e.g. Mechtley et al. 2016). In the last years, ALMA and NOEMA interferometers have expanded our knowledge of the environment around all types of QSOs by accessing a spectral regime that is mostly uncontaminated by AGN emission. Several works based on individual and small samples of high-z QSOs reported the detection of nearby sources at sub-millimetre wavelengths, e.g. Ivison et al. (2008), Clements et al. (2009), Salomé et al. (2012), Riechers (2013), Fogasy et al. (2017, 2020), Díaz-Santos et al. (2018). The discovery of companion galaxies at sub-millimetre wavelengths has been pushed to the highest redshifts ($z \sim 5$−6), revealing that ∼15−50% of luminous QSOs are accompanied by interacting companions (e.g. Decarli et al. 2017; Trakhtenbrot et al. 2017; D'Odorico et al. 2018). These companions can be as bright as the QSO host galaxies and significantly contribute to the mass growth of the host (e.g. Neeleman et al. 2019, see also Sect. 6.4). The observed high fraction of WISSH QSOs with nearby companions supports previous studies of the merger fraction as a function of AGN luminosity (e.g. Treister et al. 2012), measuring a value close to unity in bright QSOs in agreement with a major role of mergers in triggering nuclear activity. Indeed, the merger fraction appears to steeply increase with redshift (by a factor of three from $z \sim 1$ to $z \sim 2.5$) in massive galaxies such as WISSH hosts (e.g. Conselice 2014). We note that the modest angular resolution and sensitivity of our observations (see Table 1) prevent us from assessing the presence of an ongoing merger phase in all galaxies with a detected companion galaxy. Indeed, this will require to accurately probe disturbed ISM kinematics and to detect tidal features with higher angular resolution follow-up observations (e.g. see Díaz-Santos et al. 2018; Decarli et al. 2019).

6.2. Star formation efficiency and gas depletion

We investigate here the relation between CO(1−0) luminosity, tracer of the molecular gas content (e.g. Bolatto et al. 2013), and the IR luminosity, tracer of the dust-reprocessed star formation rate (e.g. Kennicutt & Evans 2012) in the host-galaxy of the WISSH QSOs. Figure 10 (left panel) displays the location of our targets in the $L_{\rm IR}$−$L'_{\rm CO(1-0)}$ plane, where $L_{\rm IR}$ is the AGN-corrected infrared luminosity (see Sect. 4). We show the best-fit relation derived for the compilation of $0 < z \lesssim 3$ main sequence galaxies by Sargent et al. (2014), indicated by the dashed line. As comparison samples, we include:

– non-lensed, luminous SMGs at $z \sim 1$−4 from Bothwell et al. (2013), starburst galaxies at $z \sim 1.5 - 2.5$ from Silverman et al. (2015), Yan et al. (2010), and dusty, highly star-forming galaxies at $z > 4$ by Fudamoto et al. (2017), for a total of 40 galaxies. In the case of Bothwell et al. (2013) targets, we distinguish between SMGs with and without AGN.
– a subsample of 36, non-lensed $z > 1$ QSOs with a good estimate of the infrared luminosity from the compilation by Perna et al. (2018). In particular, we consider QSOs with at least two photometric points in the rest-frame wavelength range 50−850 μm, and at least one detection of the far-infrared continuum within 50−200 μm, that is close to the peak of the cold dust emission. This choice limits the systematics on $L_{\rm IR}$ due to different modelling techniques and assumptions on the infrared SED (e.g. Perna et al. 2018; Kirkpatrick et al. 2019). Following the same approach used for our targets, we homogeneously compute $L'_{\rm CO(1-0)}$ of all $z > 1$ QSOs from the mid-J CO luminosity reported by Perna et al. (2018) according to the $L'_{\rm CO(J\rightarrow J-1)}/L'_{\rm CO(1-0)}$ ratios by Carilli & Walter (2013), and derive the AGN-corrected $L_{\rm IR}$ following Duras et al. (2017) for the $L_{\rm Bol} > 10^{47}$ erg s^{-1} sources.
– X-ray selected QSOs at $z \sim 2$ drawn from SUPER (SINFONI Survey for Unveiling the Physics and Effect of Radiative feedback), which have a reliable measure of $L_{\rm IR}$ (Circosta et al. 2018, and in prep.). $L'_{\rm CO(1-0)}$ and the AGN-corrected $L_{\rm IR}$ have been derived as in the previous point.

WISSH QSOs, with the exception of J1433+0227, lie below the locus of high-z, main sequence galaxies (Fig. 10). In general, the bulk of the $z > 1$ QSO population shows lower CO luminosity than MS galaxies for a given $L_{\rm IR}$, with no clear dependence on the AGN bolometric luminosity. To quantify this difference, we fit data points of WISSH QSOs and the comparison QSOs sample with a linear regression based on a Bayesian approach, by using the python package *linmix* (Kelly 2007). This allows us to consider errors on both variables $L_{\rm IR}$ and $L'_{\rm CO}$ and upper limits on the latter. For WISSH QSOs, we use the statistical uncertainty on $L_{\rm IR}$ from SED fitting (∼0.1 dex), for sources with *Herschel* plus sub-mm photometric coverage, while we consider a 0.3 dex systematic uncertainty for sources with no *Herschel* (Sect. 4). Errors on $L'_{\rm CO}$ are listed in Table 2. For the compilation of QSOs from literature, the typical uncertainties are 0.2 dex and 0.1 dex on $L_{\rm IR}$ and $L'_{\rm CO}$, respectively. The resulting best-fit correlation indicates that QSOs with infrared luminosity in the range 10^{12}−10^{13} $L_{\odot}$ (probed by WISSH QSOs and the majority of QSOs from literature) show on average a factor of ∼4 lower CO luminosity than MS galaxies. Differently, we note that the majority of SMGs follow the MS galaxies sequence, with sources below the relation being mostly associated with the presence of an AGN.

Our results provide new insights into the location of QSO host-galaxies in the $L'_{\rm CO}$−$L_{\rm IR}$ plane (e.g. Genzel et al. 2010; Carilli & Walter 2013), and are similar to findings by Perna et al. (2018), who reported a reduced CO luminosity in high-z QSOs for both obscured and unobscured sources. A different scenario was reported by Kirkpatrick et al. (2019), who performed a new, homogeneous analysis of most QSOs included in the Perna et al. (2018) collection, finding no significant difference in the $L'_{\rm CO}$−$L_{\rm IR}$ properties of QSOs and MS galaxies. Kirkpatrick et al. (2019) identified this discrepancy as mainly due to different SED fitting prescriptions at IR wavelengths and the use of a diverse CO SLED. By comparing estimates of $L_{\rm IR}$ and $L'_{\rm CO(1-0)}$ for common sources between these two works, we find most $L_{\rm IR}$ values being consistent within a factor of two, while $L'_{\rm CO(1-0)}$ is systematically higher in Kirkpatrick et al. (2019) by a factor of ∼1.5−2, and up to a factor ∼20−30 in few cases, as also shown in their Fig. 6. This is linked to the fact that Kirkpatrick et al. (2019) adopt a SMG-like CO SLED, mainly

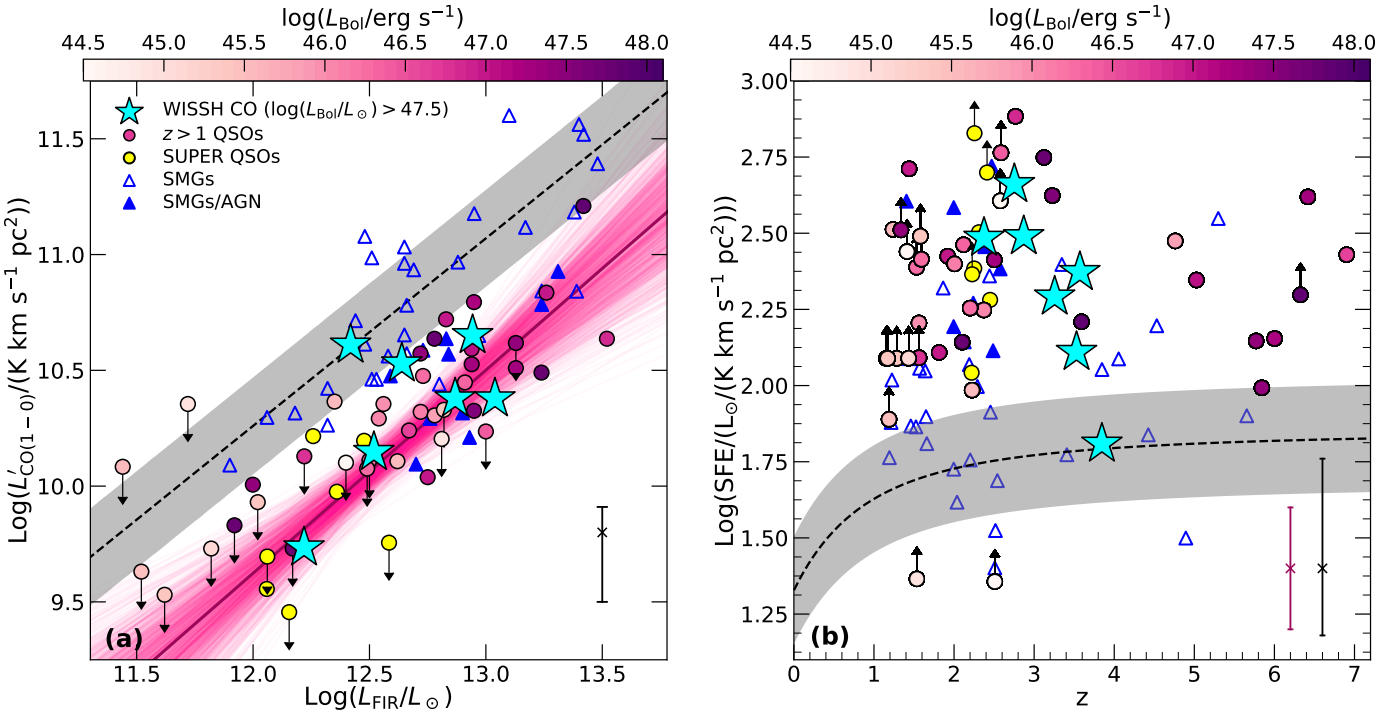

Fig. 10. *Panel a*: CO(1−0) luminosity as a function of the infrared luminosity for the WISSH QSOs analysed in this work (cyan stars), compared with a sample of QSOs and SMGs from literature (see text for details). We show the best-fit $L'_{\rm CO(1-0)}$ vs. $L_{\rm IR}$ relation measured for the QSOs sample (solid line), as compared to the relation found for MS galaxies by Sargent et al. (2014), Speagle et al. (2014) (dashed line), characterised by a 0.2 dex scatter (grey shaded area). A thousand random realisations from our Bayesian fit are also shown (pink lines). Top colorbar indicates the AGN bolometric luminosity for the $z > 1$ QSOs collection from literature. Error bar indicates the uncertainty on $L'_{\rm CO(1-0)}$ associated with the assumption of a CO SLED, given the range of CO(5−4)/CO(1−0) ratios measured in high-z QSOs (Fig. 5). *Panel b*: star formation efficiency as a function of redshift, compared to the SFE of MS galaxies with $M_* \sim 10^{11}\,M_\odot$ (black line with grey area). Black (purple) error bar indicates the typical uncertainty on SFE for WISSH targets including (without including) the systematic error on the assumption of a CO SLED (see Sect. 3.3).

obtained from CO observations of sources with low AGN fraction, while Perna et al. (2018) values reflect the different CO-SLED used in individual works, typically assuming a steeper CO-SLED (e.g. Carilli & Walter 2013). Our results (Sect. 3.3) indicate that a steeper CO SLED is more appropriate for luminous QSOs. Indeed, we note that Kirkpatrick et al. (2019) consider only CO detections, which may bias their analysis towards CO-luminous sources.

We compute the star formation efficiency in the host-galaxies of the WISSH QSOs, defined as (i) the ratio of star formation rate per molecular gas mass $\mathrm{SFE} = \mathrm{SFR}/M_{\rm gas}$ in units of yr^{-1} or, equivalently, as (ii) the ratio between the far infrared luminosity and the CO(1−0) luminosity, that is $\mathrm{SFE} = L_{\rm IR}/L'_{\rm CO(1-0)}$, in units of $L_\odot/(\mathrm{K\,km\,s^{-1}\,pc^2})$. In Fig. 10 (right panel) we adopt the second definition and show the SFE evolution as a function of redshift of the WISSH QSOs, which typically show high values of SFE in the range between 130 and 460 (hereafter in units of $L_\odot/(\mathrm{K\,km\,s^{-1}\,pc^2})$), similar to the $\mathrm{SFE} < 100$ derived in most $z > 1$ QSOs (Riechers 2011; Krips et al. 2012; Feruglio et al. 2014). In the case of J1433+0227, we measure a moderate $\mathrm{SFE} \sim 65$, consistent with the average evolution of SFE in main sequence galaxies (solid line). Specifically, we show the expected SFE–z evolutionary trend for a stellar mass $M_* = 10^{11}\,M_\odot$ from Sargent et al. (2014), Speagle et al. (2014), adapted to our empirical definition of SFE by using a CO luminosity to gas mass conversion factor $\alpha_{\rm CO} = 3.6$ (Daddi et al. 2010; Accurso et al. 2017), hereafter in units of $M_\odot/(\mathrm{K\,km\,s^{-1}\,pc^2})$, and the $L_{\rm IR}$–SFR relation from Kennicutt & Evans (2012). SMGs are characterised by a wide range of $\mathrm{SFE} \in [20, 600]$, intermediate between QSOs and MS galaxies, as also found by e.g. Magdis et al. (2012), Yang et al. (2017). We note that SMGs with AGN activity from Bothwell et al. (2013) are characterised by high SFE values, similar to the SFE of high-z QSOs. No evolution of the SFE with redshift is observed in the host-galaxy of QSOs at $1 < z < 6.5$, in agreement with previous compilation of AGN (Feruglio et al. 2014; Perna et al. 2018).

The standard approach in previous studies of molecular gas in QSOs was to assume a starburst-like conversion factor (that is $\alpha_{\rm CO} \sim 0.8$) to derive gas masses (e.g. Perna et al. 2018). This is justified by the fact that many high-z QSOs have been found to reside in highly star-forming host-galaxies, with SFR of hundreds to thousands $M_\odot\,\mathrm{yr}^{-1}$ (e.g. Solomon & Vanden Bout 2005; Carilli & Walter 2013; Combes 2018), being characterised by compact disk sizes (e.g. Brusa et al. 2018; Feruglio et al. 2018) and high molecular gas excitation (e.g. Gallerani et al. 2014; Carniani et al. 2019, see also Sect. 6.3). Several works have shown a dependence of $\alpha_{\rm CO}$ on the gas metallicity, and offset from MS, defined as $\Delta_{\rm MS} = \log(\mathrm{sSFR}/\mathrm{sSFR}_{\rm MS})$, where sSFR is the specific SFR for MS galaxies (e.g. Wolfire et al. 2010; Genzel et al. 2012; Accurso et al. 2017). Specifically, the conversion function by Accurso et al. (2017) suggests a larger $\alpha_{\rm CO} \sim 3.5$ for non-interacting galaxies with $\log(M_*/M_\odot) \sim 10.5$−$11.2$ and $\Delta_{\rm MS} \sim 0.5$, typical of the high-z QSOs sample (Sect. 6.2). However, in the case of mergers and galaxies with $\Delta_{\rm MS} > 1.3$, the starburst-like conversion factor should be used (Accurso et al. 2017; Ivison et al. 2011). Accordingly, given the evidence that ~80% of WISSH targets are in merging systems,

we adopt $\alpha_{CO} \sim 0.8$ to infer the molecular gas mass. Table 3 lists the resulting values of M_{gas}, which span about one order of magnitude from $\sim 4.4 \times 10^9\ M_\odot$ to $\sim 3.5 \times 10^{10}\ M_\odot$. This implies a variety in the properties of the molecular gas reservoirs around WISSH QSOs, consistent with previous findings in $z \sim 1-6$ QSOs (Perna et al. 2018).

Concerning J1433+0227 and J1015+0020, for which we have no CO observations, an estimate of M_{gas} can be derived by adopting a gas-to-dust ratio (GDR) and dust masses computed in Sect. 4. In low-z galaxies, a GDR ~ 100 is typically observed (e.g. Draine et al. 2007; Leroy et al. 2011). Studies of massive star forming galaxies and SMGs out to $z \sim 3-5$, comparing CO-based gas masses and dust masses obtained from far-infrared continuum emission, found a possibly increasing GDR with redshift, with typical GDR $\sim 120-250$ at $z \sim 2-4$ (e.g. Saintonge et al. 2013; Miettinen et al. 2017). In the case of WISSH QSOs, we derive gas-to-dust ratios in the range GDR $\in [100-300]$, with an average GDR $\simeq 180$ (Table 3). By adopting the latter, we obtain $\log(M_{gas}/M_\odot) \sim 11.0$ and $\log(M_{gas}/M_\odot) \sim 9.3$ for J1433+0227 and J1015+0020, respectively. An alternative approach to estimate M_{gas} consists in using the luminosity of the [CII] emission line as a tracer of the molecular gas mass. A correlation between M_{gas} and $L_{[CII]}$ has indeed been reported for $z \sim 2$ main-sequence galaxies (Zanella et al. 2018):

$$\log(M_{gas}/M_\odot) = 1.02 \times [\log(L_{[CII]}/L_\odot) + 1.28] \quad (2)$$

with a 0.3 dex scatter. By using Eq. (2) we obtain $\log(M_{gas}^{[CII]}/M_\odot) \sim 11.1$ for J1433+0227, which is almost identical to the dust-based gas mass, while the [CII]-based $\log(M_{gas}^{[CII]}/M_\odot) \sim 9.9$ in J1015+0020 is a factor of ~ 4 larger than the value inferred from M_{dust}. However, because of its low ionisation potential, [CII] simultaneously traces the molecular, atomic, and ionized gas phase (e.g. Sargsyan et al. 2012; Croxall et al. 2017). Therefore, depending on the relative contribution of the different gas phases, the total measured $L_{[CII]}$ might be higher than the one arising from the molecular gas only: this would lead to overestimated [CII]-based M_{gas}. Alternatively, dust-masses might be underestimated because of the approximation in our SED fitting that dust can be modelled by a single dust temperature (e.g. Eales et al. 2012; Aravena et al. 2016).

The ratio between the molecular gas mass and the star formation rate $\tau_{dep} = M_{gas}/SFR$ represents the gas depletion timescale (which is equivalent to 1/SFE), corresponding to the amount of time required to exhaust all the reservoir of molecular gas at the current rate of star formation. In the case of WISSH QSOs, we divide M_{gas} for the AGN-corrected SFR computed in Sect. 3.3, finding $\tau_{dep} \lesssim 100$ Myr for all sources with CO-based measure of M_{gas}, with τ_{dep} as small as $\sim 20-30$ Myr in J0209–0005, J1549+1245 and J1701+6412. Concerning the two QSOs with dust-based M_{gas}, the $\tau_{dep} \sim 20$ Myr inferred for J1015+0020 suggests that the molecular gas reservoir will be converted into stars on a similar timescale compared to the other WISSH QSOs, while in the case of J1433+0227, the large M_{gas} and modest SFR translate into a $\tau_{dep} \sim 360$ Myr. Our results indicate that all WISSH QSOs (except J1433+0227) are characterised by small τ_{dep}, shorter by an average factor of ~ 30 compared to the depletion timescale of MS galaxies of similar M_* and z. This difference cannot be explained by the uncertainty on α_{CO} only.

The high SFE and small τ_{dep} observed in WISSH QSOs might be due to starburst activity in the host-galaxies of our targets (e.g. Aravena et al. 2016; Yang et al. 2017). In fact, in the four WISSH targets for which we measure M_* (see Sect. 6.5) we find moderate offset from MS $\Delta_{MS} \sim 0.3-0.8$. Alternatively, it may be related to the impact of AGN feedback, which can reduce the molecular gas reservoir available for SF by removing and/or heating gas through the deposition of energy and momentum via AGN-driven outflows. The latter scenario will be further discussed in Sect. 6.5.

6.3. CO SLED

The relative strengths of CO emission lines with different rotational quantum numbers J, that is the CO SLED (Sect. 3.3), provide key information on the contribution of the different gas phases to the total amount of molecular gas. Specifically, low-J ($J \leq 3$) CO lines trace the cold (excitation temperature $T_{ex} \lesssim 100$ K), low-density (critical density $n_{crit} \sim 10^3-10^5$ cm^{-3}) phase, while high-J ($J \geq 5$) ones are associated with warmer and denser gas. Knowledge of the CO ladder is also necessary to convert measured high-J CO transitions in CO(1−0) luminosity, CO(1−0) being the best known tracer of molecular gas mass (M_{gas}) (e.g. Bolatto et al. 2013). It is relatively easy to probe this transition at cm wavelengths only in a minority of bright, high-z sources, as are our hyper-luminous QSOs.

The CO SLED of high redshift QSOs is still poorly known, as it has been sampled only in few sources up to $J \gtrsim 5$, including the CO(1−0) ground transition (Fig. 5). However, the studied sources are known to be affected by strong gravitational lensing (Downes et al. 1995; Venturini & Solomon 2003; Carilli et al. 2003; Lewis et al. 2002; Alloin et al. 2007), with possibly the exception of BR1202−0725 at $z \sim 4.7$ (Carilli et al. 2002; Carniani et al. 2013). Differential magnification of the CO lines emitted by different regions may therefore bias the interpretation of their SLED. Both WISSH QSOs J0209–0005 and J0801+5210, of which we investigate the CO SLED by combining CO(1−0) and CO(5−4) observations, are instead non-lensed. Specifically, SUBARU J, Ks and HST/WFC3 IR images of J0209–0005 (Wang et al. 2015) show no irregular surface brightness morphology, which may be indicative of multiple QSO images, down to an angular scale of ~ 0.2 arcsec. Similarly, in the case of J0801+5210, our inspection of g and r band images from SDSS DR12 archive showed no irregular morphology down to an angular scale of ~ 0.8 arcsec. Moreover, in the case of BR1202−0725 and the QSO MG0751+2716 (also shown in Fig. 5), the interpretation of the CO SLED might be further complicated by the presence of a radio jet (Klamer et al. 2004; Alloin et al. 2007). Similarly, ULAS J1234+0907 is characterised by strong AGN synchrotron emission (Banerji et al. 2018), while our targets show no/little AGN contribution at radio wavelengths (Sect. 4).

The CO SLED of WISSH QSOs calculated in Sect. 3.3 shows a steep rise up to $J = 5$. Specifically, the CO SLED of J0209–0005 is consistent with previous measurements of CO excitation in high-z QSOs (Carilli & Walter 2013; Casey et al. 2014), while in the case of J0801+5210 the observed CO(5−4)/CO(1−0) ratio is even higher than that expected in APM08279+5255, that is the QSO with the steepest CO SLED observed so far (Weiß et al. 2007). We note that a similarly high CO(5−4)/CO(1−0) ratio to that of J0801+5210 has been recently reported for a weakly lensed, Type 1 QSO at $z \sim 2.8$ by Fogasy et al. (2020). The high excitation of the molecular gas in our hyper-luminous targets is likely linked to AGN-related heating agents, such as X-ray photons or shocks, which influence molecular gas physics and chemistry in X-ray dominated regions (XDRs, Maloney et al. 1996). In these regions, molecular gas can be heated above 100 K (van der Werf et al. 2010; Meijerink et al. 2013;

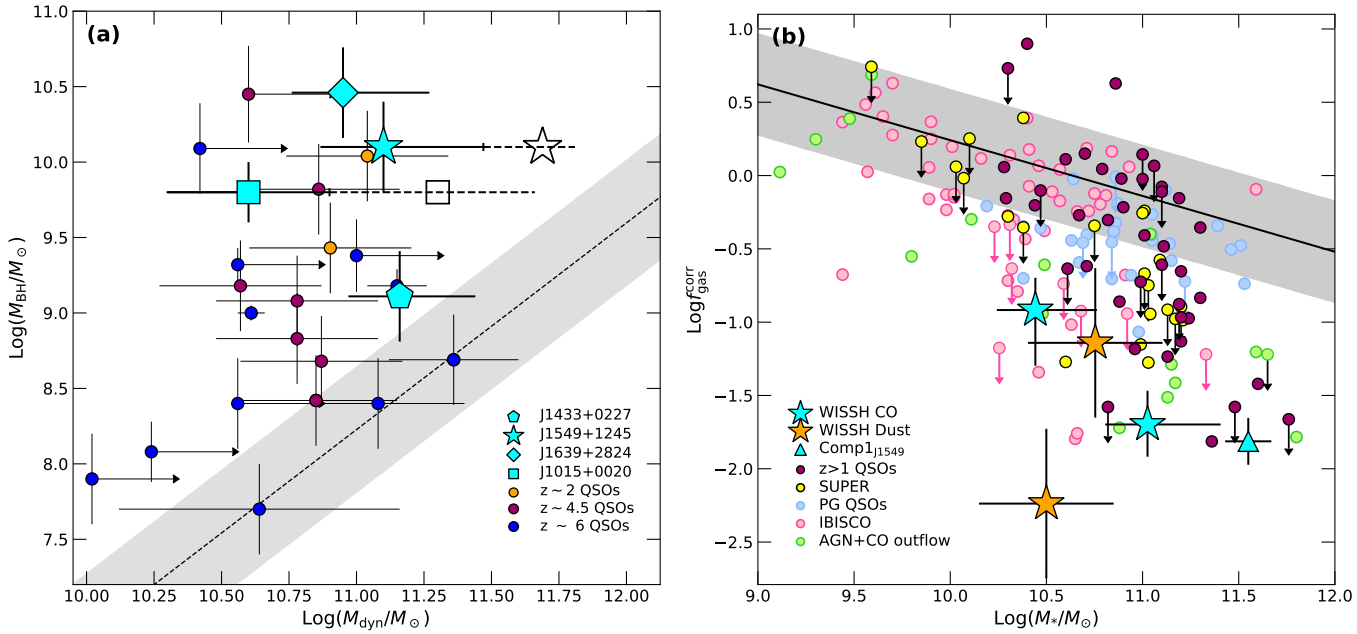

Fig. 11. *Panel a*: the black hole mass as a function of the dynamical mass of WISSH QSOs (cyan symbols), compared with $z \sim 2$–6, luminous QSOs from literature, as indicated in the legend (see text for details). The total dynamical mass associated with the QSO + companion galaxies with measured M_{dyn} are also shown by the empty symbols. For WISSH QSOs and companions (as most literature sources), M_{dyn} values are based on the FWHM of the CO or [CII] emission lines. The M_{BH}–M_{dyn} relation found for local galaxies by Jiang et al. (2011) is also indicated by the dashed line, with the associated 0.4 dex intrinsic scatter (shaded region). *Panel b*: molecular gas fraction (corrected for the dependence on redshift and offset from main-sequence) as a function of the host-galaxy stellar mass for WISSH QSOs and a compilation of high-z QSOs and local AGN (see text). WISSH QSOs with dust-based M_{gas} are indicated by orange stars. The average f_{gas}–M_* relation found for $z < 4$ star-forming galaxies from the PHIBSS survey (Tacconi et al. 2018) is shown by the solid line.

Mingozzi et al. 2018; Vallini et al. 2019; Li et al. 2020) and the high-J CO rotational energy levels become more populated with respect to photo-dissociation regions (PDRs, Hollenbach & Tielens 1999), dominated by UV photons from young stars, which mostly contribute to the CO SLED of non active, star forming galaxies (e.g. Narayanan & Krumholz 2014; Greve et al. 2014). The steep CO SLED observed in Comp$_{J0209}$ suggests that the AGN radiative output might be able to affect cold gas excitation also in nearby sources.

The limited sampling of the CO ladder in J0209–0005 and J0801+5210 as well as in their companion galaxies does not allow us to quantify the different contributions to CO excitation. Further observations of high-J CO rotational transitions, that is $J \sim 6$–10, close to the peak of the CO SLED (Mashian et al. 2015; Li et al. 2020), will be important to probe the physical properties of the molecular gas and the main excitation source in these luminous targets.

6.4. Dynamical masses

6.4.1. Size of CO and [CII] emission

In Sects. 3.2 and 5 we investigated the CO and [CII] spatial extent and kinematics of the WISSH QSOs J1433+0227, J1549+1245 and J1639+2824, in which line emission is spatially resolved by the ALMA observations. Specifically, we find the cold gas reservoir in J1433+0227, as traced by [CII] emission, to be distributed in a rotating disk with size $D = 4.4 \pm 0.3$ kpc. The latter was computed by multiplying the major axis derived in Sect. 3.2 by a factor of 1.5 (e.g. Wang et al. 2013; Venemans et al. 2016). This value is in agreement with typical sizes (2–5 kpc) of [CII] emission measured in luminous, high-z QSOs at $z \sim 4.5$–5 (Trakhtenbrot et al. 2017; Pensabene et al. 2020; Nguyen et al. 2020), and a factor of three larger than the [CII] disk size of the WISSH QSO J1015+0020 (Bischetti et al. 2018).

In the case of J1549+1245, the CO(4–3) emission is peculiarly extended over $D = 12.5 \pm 2.0$ kpc, as also observed in the companion galaxy Comp1$_{J1549}$, which is characterised by an even larger CO(4–3) size $D = 15.4 \pm 1.9$ kpc for the molecular gas reservoir. The large size measured in J1549+1245 differs from the majority of previous observations targeting mid-J CO rotational transitions in QSO host-galaxies, finding the bulk of molecular gas located in compact regions of few kpc size (e.g. Fan et al. 2018; Bischetti et al. 2019a; D'Amato et al. 2020). On the other hand, CO(3–2) emitting regions with $D >$ 10 kpc have been measured in hyper-luminous, reddened QSOs at $z \sim 2.5$ by Banerji et al. (2017), with comparable L_{Bol}. Given that several SMGs show evidence for similarly extended reservoirs but in lower excitation molecular gas (e.g. Ivison et al. 2011; Riechers et al. 2011b), this may suggest that the huge QSO radiative output in our targets is able to affect CO excitation out to tens of kpc scale and in nearby galaxies, in agreement with our findings for the CO SLED of J0209–0005 and its companion (Sect. 3.3). Concerning J1639+2824, we instead measure a compact size for the CO(4–3) emission $D = 1.7 \pm 0.2$ kpc, which is a factor of two larger than the CO size measured for this QSO by Schramm et al. (2019) from the same observation. We note that the detection of gas on larger scales might be hampered by the very high native angular resolution of the ALMA observations (Sect. 2.2).

6.4.2. Dynamical vs. SMBH mass

To calculate the dynamical mass of J1433+0227, we (a) adopt the virial relation $M_{dyn} = D v_{rot}^2 / 2G = 5.6^{+5.1}_{-1.9} \times 10^{10}\, M_\odot$, where v_{rot} is provided by the BAROLO model of the high-resolution

ALMA datacube (Sect. 5). As the BAROLO model is limited to [CII] emission from the central region with (deconvolved) size of 0.31 ± 0.03 arcsec, the virial estimate corresponds to the dynamical mass within the inner D_v = 3.5 ± 0.3 kpc; (b) use the FWHM of the [CII] emission line as a proxy of the circular velocity, according to the relation $M_{\rm dyn} = 1.16 \times 10^5 \times (0.75 \times FWHM/\sin i)^2 \times D = 1.4^{+1.3}_{-0.5} \times 10^{11}\,M_\odot$ (e.g. Wang et al. 2013; Venemans et al. 2016). Similarly, by using (b) we find $M_{\rm dyn} = 1.2^{+1.7}_{-0.5} \times 10^{11}\,M_\odot$ for J1549+1245, and a larger mass by a factor of three $M_{\rm dyn} = 3.6^{+1.1}_{-0.4} \times 10^{11}\,M_\odot$ for its companion galaxy $\mathrm{Comp1_{J1549}}$, supporting an interpretation of the QSO-companion interaction as major merger. The measured dynamical mass of J1639+2824 is $M_{\rm dyn} = 8.9^{+9.7}_{-3.2} \times 10^{10}\,M_\odot$, which is about one order of magnitude larger than the value in Schramm et al. (2019) which, however, reported their estimate of $M_{\rm dyn}$ for a rotating disk to be smaller than the black hole mass for this QSO. We point out that in the case of marginally resolved sources such as our targets, detected with moderate significance, inclination and, in turn, $M_{\rm dyn}$ estimates can be significantly altered by non-circular beam shapes. Also, non-rotating ISM components may be missed given the angular resolution of our observations. Moreover, our $M_{\rm dyn}$ are based on a single emission line whose kinematics may represent only the inner regions of the galaxy (e.g. de Blok & Walter 2014; Lupi et al. 2019). Further discussion about these issues can be found in Trakhtenbrot et al. (2017) and references therein. Finally, we note that assuming WISSH systems to be dispersion-dominated would result in smaller $M_{\rm dyn}$ by a factor of 3–4 (e.g. Decarli et al. 2018).

Both J1549+1245 and J1639+2824 benefit from single-epoch measurements of the SMBH mass ($M_{\rm BH}$) based on the Hβ λ4861 Å emission line which, being mostly dominated by virial motions, is the best estimator of $M_{\rm BH}$ (Denney 2012; Marziani & Sulentic 2012; Vietri et al. 2018) for QSOs up to $z \sim 3.8$. Specifically, Bischetti et al. (2017) and Schramm et al. (2019) found very large $\log(M_{\rm BH}/M_\odot) \simeq 10.1$–$10.4$. For the higher redshift QSO J1433+0227, a $\log(M_{\rm BH}/M_\odot) \simeq 9.11$ measured from the MgII λ2800 Å emission line was reported by Trakhtenbrot et al. (2011).

Figure 11a shows the location of the WISSH QSOs in the $M_{\rm BH}$–$M_{\rm dyn}$ plane (cyan stars), including J1015+0020 analysed in Bischetti et al. (2018). QSOs from literature with measure of $M_{\rm dyn}$ based on CO or [CII] emission lines and single epoch estimate of $M_{\rm BH}$ are also displayed. We include dusty-obscured QSOs at $z \sim 2$ from Banerji et al. (2015, 2017), Bongiorno et al. (2014), Brusa et al. (2018) and luminous $z \sim 4.5$–6 QSOs from the works of Venemans et al. (2016, 2017a), Willott et al. (2013, 2015, 2017), Kimball et al. (2015), Trakhtenbrot et al. (2017), Feruglio et al. (2018), Mortlock et al. (2011), De Rosa et al. (2014), Kashikawa et al. (2015). The $M_{\rm BH}$–$M_{\rm dyn}$ relation, derived from local galaxies in a wide range of $M_{\rm dyn} \sim 10^9$–$10^{12}\,M_\odot$ by Jiang et al. (2011), is also shown for comparison. All WISSH QSOs but J1433+0227 are characterised by a ratio between dynamical mass and SMBH mass $M_{\rm dyn}/M_{\rm BH} \sim 3$–10, among the smallest observed so far. According to the local relation, the typical $M_{\rm dyn}/M_{\rm BH}$ ratio should be ∼600 which, given the very massive black holes hosted by our targets, should translate into host-galaxy dynamical masses $\gtrsim 10^{12}\,M_\odot$. Such large values of $M_{\rm dyn}$ suggest that that hyper-luminous QSOs are the likely placeholders of high-density regions were local giant galaxies have been assembled (see also Jones et al. 2017; Díaz-Santos et al. 2018). We also note that small $M_{\rm dyn}/M_{\rm BH}$ ratios are expected in the early growth phases ($z \gtrsim 3$) of very massive BHs, for a scenario in which black-hole accretion is triggered by galaxy interactions (e.g. Lamastra et al. 2010; Menci et al. 2014).

In the case of J1549+1245, the empty star in Fig. 11a represents the total dynamical mass $\log(M_{\rm dyn}/M_\odot) \sim 11.68$ associated with the QSO plus $\mathrm{Comp1_{J1549}}$ system, under the likely hypothesis that these two sources will merge (see Sect. 3.2) and build up the mass of the QSO host-galaxy. A similar result was reported for J1015+0020 (whose mass plus that of its companion galaxy is also reported in Fig. 11a as the empty square) by Bischetti et al. (2018), who found this QSO to be associated with multiple nearby (<16 kpc) companion galaxies, for a total a $\log(M_{\rm dyn}/M_\odot) > 11$ already in place at $z \sim 4.4$. Given the widespread presence of bright companion galaxies in the surroundings of WISSH QSOs, most of which are located at close projected distance (∼6–30 kpc), we expect them to significantly contribute to the final mass of the QSO host-galaxies and consequently move the WISSH points closer to the local relation.

6.5. Gas fraction and feedback from QSO winds

To probe the amount of gas available for star-formation activity in the WISSH QSOs, we compute the molecular gas fraction, defined as $f_{\rm gas} = M_{\rm gas}/M_*$. Our targets being unobscured QSOs, a derivation of the host-galaxy stellar mass from SED fitting is particularly challenging, given that the nuclear emission outshines the galaxy at wavelengths shorter than few tens of microns (Sect. 4). An alternative approach is to infer M_* via the dynamical mass, according to the relation $M_* = M_{\rm dyn} - M_{\rm gas} - M_{\rm BH}$ (e.g. Venemans et al. 2017b; Nguyen et al. 2020), under the assumption that dark matter does not significantly contribute to the central mass of the host-galaxies (e.g. Wuyts et al. 2016). By using the latter method, we could therefore measure M_* for four of our targets and we find $\log(M_*/M_\odot) \sim 10.4$–$11.0$ and a wide range of $f_{\rm gas} \sim 0.04$–1.6 for our targets, similarly to what has been found in other high-z QSOs (e.g. Venemans et al. 2017b; Banerji et al. 2018). However, we caution that large uncertainties affect these measurements, the main of which are related to the uncertainty on the galaxy inclination and to the assumption of an $\alpha_{\rm CO}$ (Sect. 6.2). This prevents us from putting tight constraints on M_* and, in turn, on $f_{\rm gas}$. Previous studies of molecular gas content in star-forming galaxies out to $z \sim 4$ (e.g. Genzel et al. 2015; Tacconi et al. 2018) highlighted a dependence of $f_{\rm gas}$ on redshift and offset from the star-forming galaxies MS, $\Delta_{\rm MS}$. To ensure a meaningful comparison of the molecular gas fraction of WISSH QSOs with other samples at different z and $\Delta_{\rm MS}$, we thus correct $f_{\rm gas}$ for these trends. Specifically, we use the functions $f_2(z)$ and $g_2(\mathrm{sSFR/sSFR_{MS}})$ by Genzel et al. (2015), Tacconi et al. (2018), in which we parametrise $\mathrm{sSFR_{MS}}$ according to Whitaker et al. (2012).

Figure 11b shows $f_{\rm gas}^{\rm corr}$ (corrected for trends with z and $\Delta_{\rm MS}$) of WISSH QSOs as a function of M_*, compared with QSO samples as in Sect. 6.2. We also include low-redshift AGN samples, such as (i) Palomar Green (PG) QSOs with CO(2–1) based molecular gas masses (Shangguan et al. 2020); (ii) X-ray selected INTEGRAL/IBIS AGN, characterised by $\log(L_{\rm Bol}/\mathrm{erg\,s^{-1}}) \sim 43.5$–$45.6$, with CO(1–0) and CO(2–1) measurements from the IBISCO survey (Feruglio et al., in prep.). We consider (iii) active galaxies with evidence of AGN-driven molecular outflows from Fiore et al. (2017), Brusa et al. (2018), Fluetsch et al. (2019), Herrera-Camus et al. (2019). For all these sources, molecular gas masses have been homogeneously computed as in Sect. 6.2. The average $f_{\rm gas}^{\rm corr}$–M_* relation derived from ∼1400 star forming galaxies at $z < 4$ from the IRAM Plateau

de Bure HIgh-z Blue Sequence Survey (PHIBBS, Tacconi et al. 2018) is indicated by the solid line.

We find that the molecular gas fraction of WISSH QSOs is systematically smaller by a factor of ∼10−100 than that of star-forming galaxies with the same stellar mass. In general, AGN with $\log(M_*/M_\odot) < 10.25$ exhibit similar $f_{\rm gas}^{\rm corr}$ to star-forming galaxies, while at larger stellar masses the number of sources below the relation significantly increases, both in high-z QSOs and in $z \sim 0$ AGN. We note that part of the offset of WISSH QSOs (and other AGN in starbursting or merging systems, see Sect. 6.2) might be due to the adopted $\alpha_{\rm CO} = 0.8$, while the molecular gas fraction in PHIBBS galaxies is based on a complex conversion function, which takes into account metallicity and offset from MS (Genzel et al. 2015; Accurso et al. 2017). This may account for a factor of ∼4 in $f_{\rm gas}^{\rm corr}$ (error bar in Fig. 11b), given the M_* of our targets. However, even taking into account the uncertainty on $\alpha_{\rm CO}$, WISSH QSOs and ∼50% of points at $\log(M_*/M_\odot) \gtrsim 10.5$ fall short of the Tacconi et al. (2018) average $f_{\rm gas}^{\rm corr}$.

This result is in agreement with previous findings by Brusa et al. (2015), Perna et al. (2018), who reported a lower molecular gas fraction in obscured QSOs compared to MS galaxies and proposed AGN feedback as responsible for depleting the host-galaxy of the molecular gas content via outflows, during the transition, "blowout" phase from starburst galaxy to unobscured QSO (e.g. Menci et al. 2008; Hopkins et al. 2008). Moreover, Brusa et al. (2018) reported a low gas fraction in the $z \sim 1.5$ luminous, obscured QSO XID2028, in which an outflow has been detected in both the molecular and ionised gas phases (see also Cresci et al. 2015) Similarly, Fiore et al. (2017) reported a lower $f_{\rm gas}^{\rm corr}$ than MS galaxies in a collection of local AGN with evidence of molecular outflows, the gap increasing at large M_*. Carniani et al. (2017) targeted $L_{\rm Bol} \sim 10^{47}$ erg s^{-1} QSOs at $z \sim 2.4$ showing strong ionised winds, as traced by the [OIII] λ5007 Å emission line, and reported a significantly reduced gas reservoir compared to main-sequence galaxies at the same redshift. On the other hand, Herrera-Camus et al. (2019) found a $f_{\rm gas}^{\rm corr}$ consistent with the Tacconi et al. (2018) relation in a $z \sim 2.4$ QSO hosted by a massive ($M_* \sim 10^{11}\,M_\odot$), MS galaxy, with multi-phase outflows.

It is worth noting that all WISSH QSOs analysed in this work show evidence of ionised outflows, from nuclear to circum-galactic scales, as traced by large blue-shifts of their emission lines in the rest-frame UV and optical spectrum with respect to the systemic QSO redshift, as traced by CO or [CII] ($z_{\rm cold}$ in Table 2). Specifically, by analysing SDSS DR12 spectra (Alam et al. 2015) we measured the wavelength corresponding to the peak of the CIV λ1549 Å emission line ($z_{\rm SDSS}$ in Table 1), and found large velocity blue-shifts in the range $v \in [1200-5600]$ km s^{-1} with respect to the systemic redshift. Similar results were found by Vietri et al. (2018) who analysed the velocity shift between CIV and Hβ for 18 WISSH QSOs and revealed powerful, broad-line region winds with associated kinetic power $\dot{E}_{\rm kin} \sim 10^{43}-10^{44}$ erg s^{-1}. The presence of strong nuclear winds in ∼25% of the total WISSH sample was also reported in Bruni et al. (2019), who found high velocity BAL features blue-wards of CIV and SiIV λ1400 Å emission lines. Three WISSH among the targets of this work are BAL QSOs, namely J1549+1245, J1555+1003, and J1538+0855, which shows an ultra-fast BAL outflow with velocity $v \in 38\,000-47\,000$ km s^{-1}. Indeed, Bischetti et al. (2017) reported among the most powerful [OIII] outflows observed so far in five WISSH QSOs (including J1549+1245), with $\dot{E}_{\rm kin}$ up to few percent of $L_{\rm Bol}$ and extending on kpc scale, while Travascio et al. (2020) discovered a Lyα λ1216 Å outflow propagating up to ∼30 kpc in the circum-galactic medium of J1538+0855. Feedback associated with QSO activity, responsible for heating and/or removing molecular gas from the host-galaxy via outflows, is a possible scenario for the low molecular gas fractions.

We searched for the presence of cold gas outflows as traced by broad/asymmetric wings in the CO or [CII] spectra of the WISSH QSOs presented in this work. We found no detection of high-velocity cold gas. However, the limited sensitivity of our observations (Table 1) prevents us from putting meaningful upper limits on the luminosity of cold gas outflows in our targets. Indeed, molecular and neutral outflows observed in luminous QSOs typically correspond to ∼1/60 to ∼1/20 of the peak of CO and [CII] emission line profiles, respectively (e.g. Feruglio et al. 2017; Bischetti et al. 2019a,b; Cicone et al. 2015). Therefore, deeper observations in the (sub-) millimetre band are required to detect the counterpart in the cold gas phase of the powerful ionised outflows in WISSH QSOs.

7. Conclusions

We report on ALMA, NOEMA and JVLA observations of the far-infrared continuum, CO and [CII] line emission in a sample of eight hyper-luminous QSOs from the WISSH sample at $z \sim 2.4-4.7$. These data enable us to perform the first systematic study of cold gas properties in hyper-luminous QSOs at Cosmic noon. Our main findings can be summarised as follows:

- We detect CO(4−3), CO(5−4) rotational or [CII] emission in the host-galaxies of our targets (100% detection rate). In the case of J0209–0005 we also detect CO(1−0). We find CO emission to be highly excited, as suggested by the CO SLEDs of J0209–0005 and J0801+5210, among the steepest observed in high-z QSOs so far. Far-infrared and/or mm continuum is detected in ∼75% of our targets.
- For spatially resolved sources, we observe a variety of sizes for the molecular gas reservoirs, in the range ∼1.7−10 kpc. In J1433+0227, our dynamical modelling of the velocity gradient observed in the [CII] emission line indicates the presence of a fast rotating disk, in which gas motions not associated with rotation are also present. Similarly, disturbed kinematics is observed in J1549+1245 and J1639+2824.
- Our hyper-luminous QSOs are preferentially located in high-density regions, given the widespread presence of one or more line emitters around ∼80% of the QSOs. These sub-millimetre companions show bright CO or [CII] emission, in most cases comparable to emission from cold gas in the QSO host-galaxy, and are located at projected distances of ∼6−130 kpc.
- We find that the majority of WISSH QSOs exhibit a lower $L'_{\rm CO}$ (by a factor of ∼4) than $z \sim 0-3$ MS galaxies with same $L_{\rm IR}$, after correcting for the AGN contribution to infrared wavelengths. This translates into SFE $> 100\,L_\odot/$(K km s^{-1} pc^2), implying that the observed SFRs $\in [165-1095]\,M_\odot$ yr^{-1} are able to convert the molecular gas reservoir into stars on a timescale of $\lesssim$50 Myr, shorter by an average factor of ∼30 compared to the depletion timescale of MS galaxies of similar M_* and z.
- All WISSH QSOs but J1433+0227 are characterised by extremely small $M_{\rm dyn}/M_{\rm BH}$ ratios of ∼3−10, which are about two orders of magnitude offset from local relations. We find hyper-luminous QSOs to pinpoint the high-density sites where giant galaxies assemble, with significant contribution of mergers to the host-galaxy mass.

– We also infer the molecular gas fraction in the host-galaxies of four WISSH QSOs, finding lower values by a factor of ∼10−100 once compared to star forming galaxies with same M_*. This is likely linked to the widespread evidence of AGN-driven outflows in our targets having the effect of heating/depleting the gas reservoir in the galaxy.

The ALMA, JVLA and NOEMA observations analysed in this work provide a wealth of information about the properties of cold ISM and environment for a homogeneous and statistically fair sample of $L_{\rm Bol} > 10^{47}$ erg s^{-1} Type 1 QSOs shining at the peak epoch of QSO activity and massive galaxy assembly. We find these hyper-luminous objects to be caught in an evolutionary phase of concurrent intense growth of both SMBH and host-galaxy. Such growth is likely being regulated by AGN-feedback and will use up the molecular gas reservoir in few tens of Myr, supporting a scenario in which hyper-luminous QSOs are the progenitors of "red & dead" giant ellipticals. Given the richness of companion galaxies, we expect these systems to further evolve towards the local $M_{\rm BH}$−$M_{\rm dyn}$ relation via mergers.

The results presented here thus represent a critical step towards a better understanding of the SMBH-galaxy co-evolution for the objects at the extreme end of the mass function. Follow-up observations with higher angular resolution of these QSOs are needed to optimally map the cold gas kinematics in their hosts and in the companion galaxies, and better constrain the total mass and the merger state of these systems. Such observations may also be able to detect the cold gas counterparts of the ionised outflows revealed in all WISSH QSOs, assessing their multi-phase nature and global energetics.

Acknowledgements. This paper makes use of the following ALMA data: ADS/JAO.ALMA#2013.1.00417.S, ADS/JAO.ALMA#2019.1.01070.S, ADS/JAO.ALMA#2015.1.01602.S, ADS/JAO.ALMA#2016.1.00718.S, ADS/JAO.ALMA#2016.1.01515.S, ADS/JAO.ALMA#2018.1.01806.S. ALMA is a partnership of ESO (representing its member states), NSF (USA) and NINS (Japan), together with NRC (Canada), MOST and ASIAA (Taiwan), and KASI (Republic of Korea), in cooperation with the Republic of Chile. The Joint ALMA Observatory is operated by ESO, AUI/NRAO and NAOJ. This work is based on observations carried out under project number S17BW and W17DT with the IRAM NOEMA Interferometer. IRAM is supported by INSU/CNRS (France), MPG (Germany) and IGN (Spain). We are grateful to the anonymous referee for useful feedback which helped us to improve the paper. We thank Dr. Y. Wang for providing us with SUBARU images of J0209–0005 and Dr. P. Santini for useful discussion about SFE in high-z galaxies. MBi, MBr, CF, FF, AM, EP acknowledge support from PRIN MIUR project "Black Hole winds and the Baryon Life Cycle of Galaxies: the stone-guest at the galaxy evolution supper", contract #2017PH3WAT. MBi, CF and FF acknowledge support from INAF under PRIN SKA/CTA FORECaST and PRIN MAINSTREAM 2018 "Black hole winds and the baryon cycle". EP, LZ and MBi acknowledge financial support under ASI-INAF contract 2017-14-H.0. GB acknowledges financial support under the INTEGRAL ASI-INAF agreement 2019-35-HH.0 MPT acknowledges financial support from the State Agency for Research of the Spanish MCIU through the Center of Excellence Severo Ochoa award to the Instituto de Astrofísica de Andalucía (SEV-2017-0709) and through grant PGC2018-098915-B-C21 (MCI/AEI/FEDER, UE). RM acknowledges ERC Advanced Grant 695671 "QUENCH" and support by the Science and Technology Facilities Council (STFC). GVe acknowledges support from CONICYT Basal-CATA AFB-170002 and FONDECYT Postdoctorado 3200802 grants. CC acknowledges support from the Royal Society. MP is supported by the Programa Atracción de Talento de la Comunidad de Madrid via grant 2018-T2/TIC-11715. GVi acknowledges financial support from Premiale 2015 MITiC (PI B. Garilli).

References

Accurso, G., Saintonge, A., Catinella, B., et al. 2017, MNRAS, 470, 4750
Alam, S., Albareti, F. D., Allende Prieto, C., et al. 2015, ApJS, 219, 12
Alloin, D., Kneib, J. P., Guilloteau, S., & Bremer, M. 2007, A&A, 470, 53
Anglés-Alcázar, D., Faucher-Giguère, C.-A., Kereš, D., et al. 2017, MNRAS, 470, 4698
Aravena, M., Spilker, J. S., Bethermin, M., et al. 2016, MNRAS, 457, 4406
Bañados, E., Novak, M., Neeleman, M., et al. 2019, ApJ, 881, L23
Banerji, M., Alaghband-Zadeh, S., Hewett, P. C., & McMahon, R. G. 2015, MNRAS, 447, 3368
Banerji, M., Carilli, C. L., Jones, G., et al. 2017, MNRAS, 465, 4390
Banerji, M., Jones, G. C., Wagg, J., et al. 2018, MNRAS, 479, 1154
Beelen, A., Cox, P., Benford, D. J., et al. 2006, ApJ, 642, 694
Bischetti, M., Piconcelli, E., Vietri, G., et al. 2017, A&A, 598, A122
Bischetti, M., Piconcelli, E., Feruglio, C., et al. 2018, A&A, 617, A82
Bischetti, M., Piconcelli, E., Feruglio, C., et al. 2019a, A&A, 628, A118
Bischetti, M., Maiolino, R., Carniani, S., et al. 2019b, A&A, 630, A59
Bolatto, A. D., Wolfire, M., & Leroy, A. K. 2013, ARA&A, 51, 207
Bongiorno, A., Maiolino, R., Brusa, M., et al. 2014, MNRAS, 443, 2077
Bothwell, M. S., Smail, I., Chapman, S. C., et al. 2013, MNRAS, 429, 3047
Briggs, D. S. 1995, Am. Astron. Soc. Meet. Abstr., 187, 112.02
Bruni, G., Piconcelli, E., Misawa, T., et al. 2019, A&A, 630, A111
Brusa, M., Feruglio, C., Cresci, G., et al. 2015, A&A, 578, A11
Brusa, M., Cresci, G., Daddi, E., et al. 2018, A&A, 612, A29
Carilli, C. L., & Walter, F. 2013, ARA&A, 51, 105
Carilli, C. L., Kohno, K., Kawabe, R., et al. 2002, AJ, 123, 1838
Carilli, C. L., Lewis, G. F., Djorgovski, S. G., et al. 2003, Science, 300, 773
Carniani, S., Marconi, A., Biggs, A., et al. 2013, A&A, 559, A29
Carniani, S., Marconi, A., Maiolino, R., et al. 2015, A&A, 580, A102
Carniani, S., Marconi, A., Maiolino, R., et al. 2017, A&A, 605, A105
Carniani, S., Gallerani, S., Vallini, L., et al. 2019, MNRAS, 489, 3939
Casey, C. M., Narayanan, D., & Cooray, A. 2014, Phys. Rep., 541, 45
Choi, E., Somerville, R. S., Ostriker, J. P., Naab, T., & Hirschmann, M. 2018, ApJ, 866, 91
Cicone, C., Maiolino, R., Gallerani, S., et al. 2015, A&A, 574, A14
Circosta, C., Mainieri, V., Padovani, P., et al. 2018, A&A, 620, A82
Clements, D. L., Petitpas, G., Farrah, D., et al. 2009, ApJ, 698, L188
Coatman, L., Hewett, P. C., Banerji, M., et al. 2017, MNRAS, 465, 2120
Combes, F. 2018, A&ARv, 26, 5
Conselice, C. J. 2014, ARA&A, 52, 291
Cresci, G., Mainieri, V., Brusa, M., et al. 2015, ApJ, 799, 82
Croton, D. J., Springel, V., White, S. D. M., et al. 2006, MNRAS, 365, 11
Croxall, K. V., Smith, J. D., Pellegrini, E., et al. 2017, ApJ, 845, 96
Daddi, E., Elbaz, D., Walter, F., et al. 2010, ApJ, 714, L118
D'Amato, Q., Gilli, R., Vignali, C., et al. 2020, A&A, 636, A37
Davies, R., Förster Schreiber, N. M., Cresci, G., et al. 2011, ApJ, 741, 69
de Blok, W. J. G., & Walter, F. 2014, AJ, 147, 96
Decarli, R., Walter, F., Venemans, B. P., et al. 2017, Nature, 545, 457
Decarli, R., Walter, F., Venemans, B. P., et al. 2018, ApJ, 854, 97
Decarli, R., Dotti, M., Bañados, E., et al. 2019, ApJ, 880, 157
Delvecchio, I., Gruppioni, C., Pozzi, F., et al. 2014, MNRAS, 439, 2736
Denney, K. D. 2012, ApJ, 759, 44
De Rosa, G., Venemans, B. P., Decarli, R., et al. 2014, ApJ, 790, 145
Díaz-Santos, T., Assef, R. J., Blain, A. W., et al. 2016, ApJ, 816, L6
Díaz-Santos, T., Assef, R. J., Blain, A. W., et al. 2018, Science, 362, 1034
Di Matteo, P., Combes, F., Melchior, A. L., & Semelin, B. 2007, A&A, 468, 61
Di Teodoro, E. M., & Fraternali, F. 2015, MNRAS, 451, 3021
D'Odorico, V., Feruglio, C., Ferrara, A., et al. 2018, ApJ, 863, L29
Downes, D., Solomon, P. M., & Radford, S. J. E. 1995, ApJ, 453, L65
Draine, B. T., Dale, D. A., Bendo, G., et al. 2007, ApJ, 663, 866
Dunne, L., Eales, S., Edmunds, M., et al. 2000, MNRAS, 315, 115
Duras, F., Bongiorno, A., Piconcelli, E., et al. 2017, A&A, 604, A67
Eales, S., Smith, M. W. L., Auld, R., et al. 2012, ApJ, 761, 168
Fan, L., Han, Y., Fang, G., et al. 2016, ApJ, 822, L32
Fan, L., Knudsen, K. K., Fogasy, J., & Drouart, G. 2018, ApJ, 856, L5
Fan, L., Knudsen, K. K., Han, Y., & Tan, Q.-H. 2019, ApJ, 887, 74
Feltre, A., Hatziminaoglou, E., Fritz, J., & Franceschini, A. 2012, MNRAS, 426, 120
Feruglio, C., Bongiorno, A., Fiore, F., et al. 2014, A&A, 565, A91
Feruglio, C., Ferrara, A., Bischetti, M., et al. 2017, A&A, 608, A30
Feruglio, C., Fiore, F., Carniani, S., et al. 2018, A&A, 619, A39
Fiore, F., Feruglio, C., Shankar, F., et al. 2017, A&A, 601, A143
Fluetsch, A., Maiolino, R., Carniani, S., et al. 2019, MNRAS, 483, 4586
Fogasy, J., Knudsen, K. K., Lagos, C. D. P., Drouart, G., & Gonzalez-Perez, V. 2017, A&A, 597, A123
Fogasy, J., Knudsen, K. K., Drouart, G., Lagos, C. D. P., & Fan, L. 2020, MNRAS, 493, 3744
Förster Schreiber, N. M., Genzel, R., Bouché, N., et al. 2009, ApJ, 706, 1364
Fudamoto, Y., Ivison, R. J., Oteo, I., et al. 2017, MNRAS, 472, 2028
Gallerani, S., Ferrara, A., Neri, R., & Maiolino, R. 2014, MNRAS, 445, 2848
Genzel, R., Tacconi, L. J., Gracia-Carpio, J., et al. 2010, MNRAS, 407, 2091
Genzel, R., Tacconi, L. J., Combes, F., et al. 2012, ApJ, 746, 69
Genzel, R., Tacconi, L. J., Lutz, D., et al. 2015, ApJ, 800, 20
Glikman, E., Simmons, B., Mailly, M., et al. 2015, ApJ, 806, 218
Greve, T. R., Leonidaki, I., Xilouris, E. M., et al. 2014, ApJ, 794, 142

Griffin, M. J., Abergel, A., Abreu, A., et al. 2010, A&A, 518, L3
Häring, N., & Rix, H.-W. 2004, ApJ, 604, L89
Helfand, D. J., White, R. L., & Becker, R. H. 2015, ApJ, 801, 26
Herrera-Camus, R., Tacconi, L., Genzel, R., et al. 2019, ApJ, 871, 37
Herrera-Camus, R., Janssen, A., Sturm, E., et al. 2020, A&A, 635, A47
Högbom, J. A. 1974, A&AS, 15, 417
Hollenbach, D. J., & Tielens, A. G. G. M. 1999, Rev. Mod. Phys., 71, 173
Hopkins, P. F. 2012, MNRAS, 420, L8
Hopkins, P. F., Hernquist, L., Cox, T. J., & Kereš, D. 2008, ApJS, 175, 356
Ivison, R. J., Morrison, G. E., Biggs, A. D., et al. 2008, MNRAS, 390, 1117
Ivison, R. J., Papadopoulos, P. P., Smail, I., et al. 2011, MNRAS, 412, 1913
Jiang, Y.-F., Greene, J. E., & Ho, L. C. 2011, ApJ, 737, L45
Jones, S. F., Blain, A. W., Assef, R. J., et al. 2017, MNRAS, 469, 4565
Kakkad, D., Mainieri, V., Brusa, M., et al. 2017, MNRAS, 468, 4205
Kakkad, D., Mainieri, V., Vietri, G., et al. 2020, A&A, 642, A147
Kashikawa, N., Ishizaki, Y., Willott, C. J., et al. 2015, ApJ, 798, 28
Kelly, B. C. 2007, ApJ, 665, 1489
Kennicutt, R. C., Jr. 1998, ApJ, 498, 541
Kennicutt, R. C., & Evans, N. J. 2012, ARA&A, 50, 531
Kimball, A. E., Lacy, M., Lonsdale, C. J., & Macquart, J. P. 2015, MNRAS, 452, 88
King, A., & Pounds, K. 2015, ARA&A, 53, 115
Kirkpatrick, A., Sharon, C., Keller, E., & Pope, A. 2019, ApJ, 879, 41
Klamer, I. J., Ekers, R. D., Sadler, E. M., & Hunstead, R. W. 2004, ApJ, 612, L97
Kormendy, J., & Ho, L. C. 2013, ARA&A, 51, 511
Krips, M., Neri, R., & Cox, P. 2012, ApJ, 753, 135
Lamastra, A., Menci, N., Maiolino, R., Fiore, F., & Merloni, A. 2010, MNRAS, 405, 29
Leroy, A. K., Bolatto, A., Gordon, K., et al. 2011, ApJ, 737, 12
Lewis, G. F., Carilli, C., Papadopoulos, P., & Ivison, R. J. 2002, MNRAS, 330, L15
Li, J., Wang, R., Riechers, D., et al. 2020, ApJ, 889, 162
Lupi, A., Volonteri, M., Decarli, R., et al. 2019, MNRAS, 488, 4004
Lusso, E., Comastri, A., Simmons, B. D., et al. 2012, MNRAS, 425, 623
Magdis, G. E., Daddi, E., Béthermin, M., et al. 2012, ApJ, 760, 6
Maiolino, R., Gallerani, S., Neri, R., et al. 2012, MNRAS, 425, L66
Maloney, P. R., Hollenbach, D. J., & Tielens, A. G. G. M. 1996, ApJ, 466, 561
Marconi, A., Risaliti, G., Gilli, R., et al. 2004, MNRAS, 351, 169
Martín-Navarro, I., Brodie, J. P., Romanowsky, A. J., Ruiz-Lara, T., & van de Ven, G. 2018, Nature, 553, 307
Marziani, P., & Sulentic, J. W. 2012, New Astron. Rev., 56, 49
Mashian, N., Sturm, E., Sternberg, A., et al. 2015, ApJ, 802, 81
McDermid, R. M., Alatalo, K., Blitz, L., et al. 2015, MNRAS, 448, 3484
McMullin, J. P., Waters, B., Schiebel, D., Young, W., & Golap, K. 2007, in Astronomical Data Analysis Software and Systems XVI, eds. R. A. Shaw, F. Hill, & D. J. Bell, ASP Conf. Ser., 376, 127
Mechtley, M., Jahnke, K., Windhorst, R. A., et al. 2016, ApJ, 830, 156
Meijerink, R., Kristensen, L. E., Weiß, A., et al. 2013, ApJ, 762, L16
Menci, N., Fiore, F., Puccetti, S., & Cavaliere, A. 2008, ApJ, 686, 219
Menci, N., Gatti, M., Fiore, F., & Lamastra, A. 2014, A&A, 569, A37
Menci, N., Fiore, F., Feruglio, C., et al. 2019, ApJ, 877, 74
Miettinen, O., Delvecchio, I., Smolčić, V., et al. 2017, A&A, 606, A17
Mingozzi, M., Vallini, L., Pozzi, F., et al. 2018, MNRAS, 474, 3640
Mortlock, D. J., Warren, S. J., Venemans, B. P., et al. 2011, Nature, 474, 616
Narayanan, D., & Krumholz, M. R. 2014, MNRAS, 442, 1411
Neeleman, M., Bañados, E., Walter, F., et al. 2019, ApJ, 882, 10
Nguyen, N. H., Lira, P., Trakhtenbrot, B., et al. 2020, ApJ, 895, 74
Pensabene, A., Carniani, S., Perna, M., et al. 2020, A&A, 637, A84
Perna, M., Sargent, M. T., Brusa, M., et al. 2018, A&A, 619, A90
Perrotta, S., Hamann, F., Zakamska, N. L., et al. 2019, MNRAS, 488, 4126
Pilbratt, G. L., Riedinger, J. R., Passvogel, T., et al. 2010, A&A, 518, L1
Planck Collaboration XIII. 2016, A&A, 594, A13
Richings, A. J., & Faucher-Giguère, C.-A. 2018, MNRAS, 478, 3100
Riechers, D. A. 2011, ApJ, 730, 108
Riechers, D. A. 2013, ApJ, 765, L31
Riechers, D. A., Carilli, C. L., Maddalena, R. J., et al. 2011a, ApJ, 739, L32
Riechers, D. A., Hodge, J., Walter, F., Carilli, C. L., & Bertoldi, F. 2011b, ApJ, 739, L31
Saintonge, A., Lutz, D., Genzel, R., et al. 2013, ApJ, 778, 2
Salomé, P., Guélin, M., Downes, D., et al. 2012, A&A, 545, A57
Santini, P., Fontana, A., Grazian, A., et al. 2009, A&A, 504, 751
Sargent, M. T., Daddi, E., Béthermin, M., et al. 2014, ApJ, 793, 19
Sargsyan, L., Lebouteiller, V., Weedman, D., et al. 2012, ApJ, 755, 171
Schramm, M., Rujopakarn, W., Silverman, J. D., et al. 2019, ApJ, 881, 145
Scoville, N., Sheth, K., Aussel, H., et al. 2016, ApJ, 820, 83
Shangguan, J., Ho, L. C., Bauer, F. E., Wang, R., & Treister, E. 2020, ApJS, 247, 15
Shankar, F., Bernardi, M., Richardson, K., et al. 2019, MNRAS, 485, 1278
Shen, Y. 2016, ApJ, 817, 55
Shen, Y., Richards, G. T., Strauss, M. A., et al. 2011, ApJS, 194, 45
Sijacki, D., Springel, V., Di Matteo, T., & Hernquist, L. 2007, MNRAS, 380, 877
Silverman, J. D., Daddi, E., Rodighiero, G., et al. 2015, ApJ, 812, L23
Skrutskie, M. F., Cutri, R. M., Stiening, R., et al. 2006, AJ, 131, 1163
Solomon, P. M., & Vanden Bout, P. A. 2005, ARA&A, 43, 677
Speagle, J. S., Steinhardt, C. L., Capak, P. L., & Silverman, J. D. 2014, ApJS, 214, 15
Stalevski, M., Ricci, C., Ueda, Y., et al. 2016, MNRAS, 458, 2288
Symeonidis, M. 2017, MNRAS, 465, 1401
Tacconi, L. J., Neri, R., Genzel, R., et al. 2013, ApJ, 768, 74
Tacconi, L. J., Genzel, R., Saintonge, A., et al. 2018, ApJ, 853, 179
Talia, M., Pozzi, F., Vallini, L., et al. 2018, MNRAS, 476, 3956
Trakhtenbrot, B., Netzer, H., Lira, P., & Shemmer, O. 2011, ApJ, 730, 7
Trakhtenbrot, B., Lira, P., Netzer, H., et al. 2017, ApJ, 836, 8
Travascio, A., Zappacosta, L., Cantalupo, S., et al. 2020, A&A, 635, A157
Treister, E., Schawinski, K., Urry, C. M., & Simmons, B. D. 2012, ApJ, 758, L39
Urrutia, T., Lacy, M., & Becker, R. H. 2008, ApJ, 674, 80
Vallini, L., Tielens, A. G. G. M., Pallottini, A., et al. 2019, MNRAS, 490, 4502
van der Werf, P. P., Isaak, K. G., Meijerink, R., et al. 2010, A&A, 518, L42
van de Voort, F. 2017, in The Effect of Galactic Feedback on Gas Accretion and Wind Recycling, eds. A. Fox, & R. Davé, Astrophys. Space Sci. Lib., 430, 301
Veilleux, S., Maiolino, R., Bolatto, A. D., & Aalto, S. 2020, A&ARv, 28, 2
Venemans, B. P., Walter, F., Zschaechner, L., et al. 2016, ApJ, 816, 37
Venemans, B. P., Walter, F., Decarli, R., et al. 2017a, ApJ, 837, 146
Venemans, B. P., Walter, F., Decarli, R., et al. 2017b, ApJ, 845, 154
Venemans, B. P., Neeleman, M., Walter, F., et al. 2019, ApJ, 874, L30
Venturini, S., & Solomon, P. M. 2003, ApJ, 590, 740
Vietri, G., Piconcelli, E., Bischetti, M., et al. 2018, A&A, 617, A81
Villar Martín, M., Perna, M., Humphrey, A., et al. 2020, A&A, 634, A116
Volonteri, M., Capelo, P. R., Netzer, H., et al. 2015, MNRAS, 449, 1470
Wang, R., Wagg, J., Carilli, C. L., et al. 2013, ApJ, 773, 44
Wang, Y.-P., He, W., Yamada, T., et al. 2015, Res. Astron. Astrophys., 15, 673
Wang, R., Wu, X.-B., Neri, R., et al. 2016, ApJ, 830, 53
Weedman, D., Sargsyan, L., Lebouteiller, V., Houck, J., & Barry, D. 2012, ApJ, 761, 184
Weiß, A., Downes, D., Neri, R., et al. 2007, A&A, 467, 955
Whitaker, K. E., van Dokkum, P. G., Brammer, G., & Franx, M. 2012, ApJ, 754, L29
Willott, C. J., Omont, A., & Bergeron, J. 2013, ApJ, 770, 13
Willott, C. J., Bergeron, J., & Omont, A. 2015, ApJ, 801, 123
Willott, C. J., Bergeron, J., & Omont, A. 2017, ApJ, 850, 108
Wolfire, M. G., Hollenbach, D., & McKee, C. F. 2010, ApJ, 716, 1191
Wright, E. L., Eisenhardt, P. R. M., Mainzer, A. K., et al. 2010, AJ, 140, 1868
Wuyts, S., Förster Schreiber, N. M., Wisnioski, E., et al. 2016, ApJ, 831, 149
Wylezalek, D., Zakamska, N. L., Liu, G., & Obied, G. 2016, MNRAS, 457, 745
Yan, L., Tacconi, L. J., Fiolet, N., et al. 2010, ApJ, 714, 100
Yang, C., Omont, A., Beelen, A., et al. 2017, A&A, 608, A144
Yun, M. S., & Carilli, C. L. 2002, ApJ, 568, 88
Zakamska, N. L., Hamann, F., Pâris, I., et al. 2016, MNRAS, 459, 3144
Zanella, A., Daddi, E., Magdis, G., et al. 2018, MNRAS, 481, 1976
Zappacosta, L., Piconcelli, E., Duras, F., et al. 2018, A&A, 618, A28

[1] INAF – Osservatorio Astronomico di Trieste, Via G. B. Tiepolo 11, 34143 Trieste, Italy
e-mail: manuela.bischetti@inaf.it
[2] INAF – Osservatorio Astronomico di Roma, Via Frascati 33, 00078 Monte Porzio Catone, Italy
[3] Dipartimento di Matematica e Fisica, Universitá Roma Tre, Via della Vasca Navale 84, 00146 Roma, Italy
[4] Instituto de Astrofísica de Andalucía (IAA, CSIC), Glorieta de las Astronomía, s/n, 18008 Granada, Spain
[5] Departamento de Física Teorica, Facultad de Ciencias, Universidad de Zaragoza, Zaragoza, Spain
[6] European Southern Observatory (ESO), Alonso de Córdova 3107, Vitacura, Casilla 19001, Santiago de Chile, Chile
[7] Institute of Space Sciences (ICE, CSIC), Campus UAB, Carrer de Magrans, 08193 Barcelona, Spain
[8] Instituto de Astrofísica, Pontificia Universidad Católica de Chile, Avda Vicuna Mackenna 4860, 8970117 Macul, Santiago, Chile
[9] Scuola Normale Superiore, Piazza dei Cavalieri 7, 56126 Pisa, Italy

[10] INAF – Istituto di Astrofisica e Planetologia Spaziali, Via Fosso del Cavaliere 100, 00133 Roma, Italy
[11] Dpto. de Ciencias Fisicas, Universidad Andres Bello, Campus La Casona, Fernandez Concha 700, 7500912 Santiago, Chile
[12] Dipartimento di Fisica e Astronomia, Alma Mater Studiorum Universitá di Bologna, Via Gobetti 93/2, 40129 Bologna, Italy
[13] INAF – Osservatorio di Astrofisica e Scienza dello Spazio di Bologna, Via Gobetti 93/3, 40129 Bologna, Italy
[14] Department of Physics & Astronomy, University College London, Gower Street, London WC1E 6BT, UK
[15] INAF-Osservatorio Astrofisico di Arcetri, Largo E. Fermi 2, 50125 Firenze, Italy
[16] Kavli Institute for Cosmology, University of Cambridge, Madingley Road, Cambridge CB3 0HA, UK
[17] Cavendish Laboratory, University of Cambridge, 19 J. J. Thomson Avenue, Cambridge CB3 0HE, UK
[18] Dipartimento di Fisica e Astronomia, Universitá degli Studi di Firenze, Via G. Sansone 1, 50019 Sesto Fiorentino, Firenze, Italy
[19] INAF – Padova Astronomical Observatory, Vicolo dell'Osservatorio 5, 35122 Padova, Italy
[20] Instituto de Astrofísica e Ciências do Espaço, Universidade de Lisboa, OAL, Tapada da Ajuda, 1349-018 Lisboa, Portugal
[21] Centro de Astrobiología (CAB, CSIC-INTA), Dpto. de Astrofísica, Ctra de Ajalvir km 4, 28850 Torrejón de Ardoz, Madrid, Spain
[22] Max-Planck-Institut für Radioastronomie, Auf dem Hügel 69, 53121 Bonn, Germany
[23] INAF – Istituto di Astrofisica Spaziale e Fisica Cosmica Milano, Via A. Corti 12, 20133 Milano, Italy

Appendix A: Broad-band UV-to-FIR SEDs of WISSH QSOs

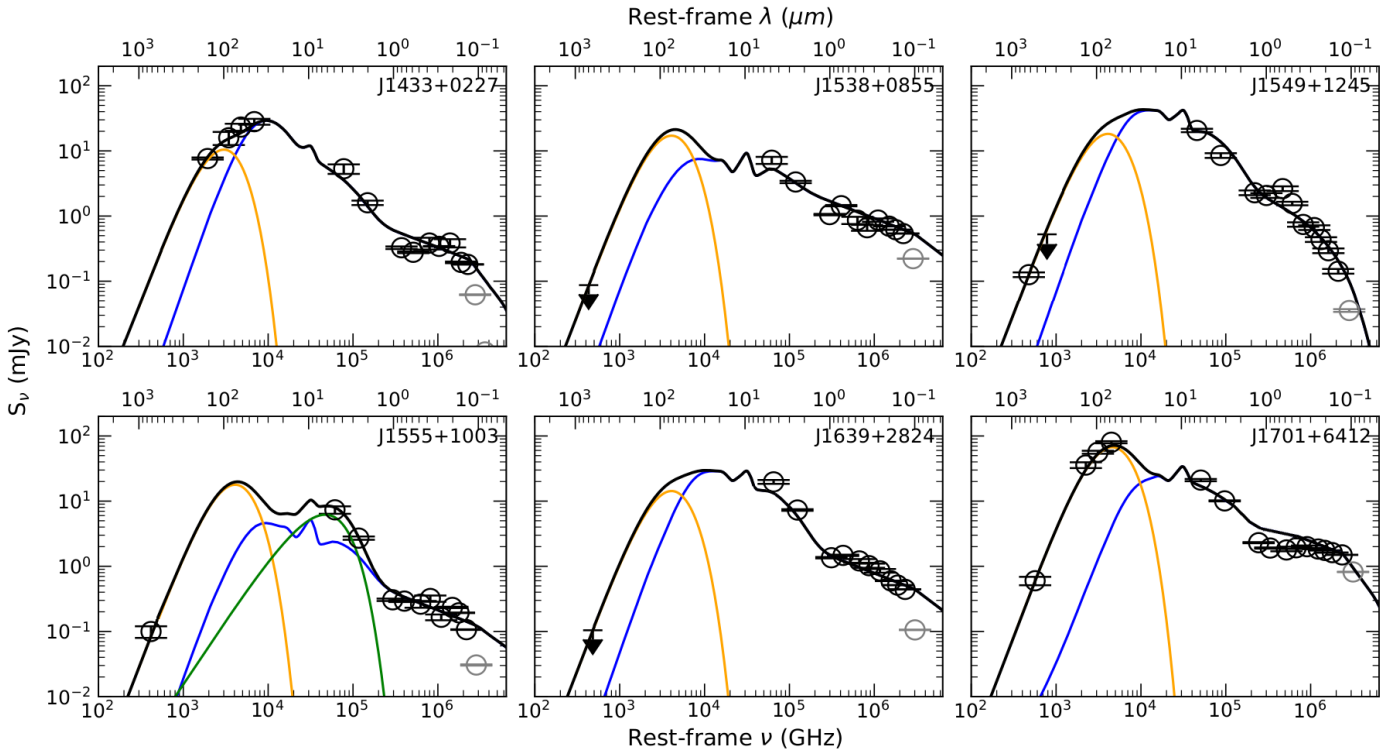

Fig. A.1. Rest-frame SED of the WISSH QSOs considered in this work. In each panel, black symbols indicate the photometric points considered in our modelling. Black circles identify detections while arrows represent 3σ upper limits (see Table 1). Photometric points at $\lambda < 1216$ Å are not included in the fits due to Lyα absorption (grey circles). Black curve represents the total best fit model, while blue and orange curves refer to the accretion disk plus torus and cold dust emission, respectively. In the case of J1555+1003, the green curve represents the best-fit template reproducing the near-IR excess (for details, see Duras et al. 2017).